



Universidade Estadual de Maringá
Centro de Ciências Biológicas
Programa de Pós-Graduação em Ciências Biológicas
Área de Concentração: Biologia Celular e Molecular



FRANCIELLE PELEGRIN GARCIA GEREMIAS

**MORTE CELULAR DE *Leishmania amazonensis* INDUZIDA POR
(1E,4E)-2-METIL-1,5-BIS(4-NITROFENIL)PENTA-1,4-DIEN-3-ONA
E DESENVOLVIMENTO DE NANOGÉIS A BASE DE ÁCIDO
HIALURÔNICO COMO CARREADORES DE SUBSTÂNCIAS
HIDROFÓBICAS BIOATIVAS**

Maringá

2017



Universidade Estadual de Maringá
Centro de Ciências Biológicas
Programa de Pós-Graduação em Ciências Biológicas
Área de Concentração: Biologia Celular e Molecular



FRANCIELLE PELEGRIN GARCIA GEREMIAS

**MORTE CELULAR DE *Leishmania amazonensis* INDUZIDA POR
(1E,4E)-2-METIL-1,5-BIS(4-NITROFENIL)PENTA-1,4-DIEN-3-ONA
E DESENVOLVIMENTO DE NANOGÉIS A BASE DE ÁCIDO
HIALURÔNICO COMO CARREADORES DE SUBSTÂNCIAS
HIDROFÓBICAS BIOATIVAS**

Tese apresentada ao Programa de Pós-Graduação em Ciências Biológicas (Área de Concentração – Biologia Celular e Molecular) da Universidade Estadual de Maringá, para a obtenção do grau de doutor em Ciências Biológicas.

Maringá

Junho - 2017

Francielle Pelegrin Garcia Geremias

**MORTE CELULAR DE *Leishmania amazonensis* INDUZIDA POR
(1E,4E)-2-METIL-1,5-BIS(4-NITROFENIL)PENTA-1,4-DIEN-3-ONA
E DESENVOLVIMENTO DE NANOGÉIS A BASE DE ÁCIDO
HIALURÔNICO COMO CARREADORES DE SUBSTÂNCIAS
HIDROFÓBICAS BIOATIVAS**

Orientador: Prof. Dr. Celso Vataru Nakamura

AGRADECIMENTOS

Em primeiro lugar gostaria de agradecer à Deus, por me guiar, dar sabedoria e tranquilidade para seguir em frente com os meus objetivos e não desanimar com as dificuldades. Agradeço ainda por Ele ter colocado em minha vida tantas pessoas especiais que me ajudaram nessa caminhada:

Meus pais, meu marido e toda a minha família, por estarem sempre ao meu lado e por terem sempre feito tudo para que eu alcançasse todos os meus objetivos, além de me apoiarem e me incentivarem a superar meus limites a cada dia;

Professor Celso, por todas as oportunidades concedidas, pela confiança depositada em mim e por todos esses anos de aprendizado e dedicação;

Professora Rachel, por me aceitar em seu laboratório, pela paciência e por compartilhar seus conhecimentos, me proporcionando uma experiência incrível no exterior;

À todos os amigos do Laboratório de Inovação Tecnológica no Desenvolvimento de Fármacos e Cosméticos, pela convivência, parceria e amizade;

À Universidade Estadual de Maringá, ao Programa de Pós Graduação em Ciências Biológicas e à CAPES, pela oportunidade, conhecimentos adquiridos e pelo auxílio financeiro.

Por fim, agradeço a todos que, de alguma forma, perto ou longe, torceram e contribuíram para que eu chegasse até aqui!

Muito obrigada a todos!

APRESENTAÇÃO

Esta tese é composta de um resumo geral, em português e inglês, e dois artigos científicos. O primeiro artigo, intitulado “**A3K2A3-induced Apoptotic Cell Death of *Leishmania amazonensis* Occurs Through Caspase- and ATP-dependent Mitochondrial Dysfunction**”, aborda as principais metodologias utilizadas para investigar o mecanismo de ação da substância A3K2A3 envolvido na morte celular desse parasito visto sua interessante atividade antileishmania previamente descrita. Em consonância com as regras do Programa de Pós-graduação em Ciências Biológicas, o artigo foi redigido de acordo com as normas da revista Apoptosis. O segundo artigo, intitulado “**Tuning the stability of self-assembled nanogels based on hyaluronic acid using ketone-hydrazide cross-linking**” aborda a síntese, caracterização e aplicação biológica em modelos tumorais de nanogéis termorresponsíveis que podem ser utilizados como carreadores de moléculas hidrofóbicas. O artigo foi escrito conforme as normas da revista Biomacromolecules.

Garcia, F. P., da Silva Rodrigues, J. H., Din, Z. U., Rodrigues-Filho, E., Ueda-Nakamura, T., Auzély-Velty, R., & Nakamura, C. V. (2017). A3K2A3-induced apoptotic cell death of *Leishmania amazonensis* occurs through caspase-and ATP-dependent mitochondrial dysfunction. Apoptosis, 1-15. DOI: 10.1007/s10495-016-1308-4

Garcia, F. P., Vianna, M., Stefanello T.F., Rippe, M, Louage B., De Geest B.G., Sancey L., Coll J.L., Nakamura, C. V. Auzély-Velty, R. Tuning the stability of self-assembled nanogels based on hyaluronic acid using ketone-hydrazide cross-linking.

RESUMO GERAL

INTRODUÇÃO E OBJETIVOS: As leishmanioses são um complexo de doenças com importante espectro clínico e diversidade epidemiológica, representando um grave problema de saúde pública em todo o mundo. Por se tratar de uma doença negligenciada, apesar do progresso em conhecimentos fundamentais sobre o parasito, o tratamento atual contra a leishmaniose ainda é insatisfatório, devido à eficácia limitada, aumento de casos de resistência, além do longo tempo de tratamento e efeitos colaterais. Assim, considerando o potencial antileishmania já descrito para derivados de chalconas, a substância (1E,4E)-2-metil-1,5-bis(4-nitrofenil)penta-1,4-dien-3-ona (A3K2A3) apresentou-se como uma candidata promissora em testes *in vitro* preliminares. Neste contexto, desenvolvemos um estudo mais aprofundado dessa atividade, bem como de seu possível mecanismo de ação associado a morte celular dos parasitos. Entretanto, este derivado de chalcona, bem como parte considerável das novas substâncias, apresentam elevada hidrofobicidade, a qual normalmente se associam diversos problemas de administração *in vivo*, como baixa absorção e biodisponibilidade sistêmica, agregação intravenosa, entre outros efeitos, podendo limitar seu potencial biológico. Dessa forma, para se obter um melhor resultado no tratamento contra as doenças infecciosas é necessário não apenas investigar novos compostos que possuam potencial terapêutico, mas também incorporá-los a novas tecnologias, tais como nanopartículas, as quais permitam um aumento da atividade biológica, maior biodisponibilidade e estabilidade em meio fisiológico, além de redução de possíveis efeitos colaterais e uma melhor abordagem terapêutica aos pacientes. Neste contexto, o objetivo deste trabalho foi a realização de um estudo *in vitro* para compreender a atividade e o mecanismo de ação da substância A3K2A3 envolvido na morte celular desses parasitos bem como o desenvolvimento de nanogéis a base de ácido hialurônico como carreadores de substâncias hidrofóbicas para células alvo.

MÉTODOS, RESULTADOS E DISCUSSÃO: Inicialmente, foram realizados estudos da atividade de A3K2A3 sobre formas promastigotas e amastigotas intracelulares de *Leishmania amazonensis* e ainda sua citotoxicidade *in vitro* sobre hemácias. Resultados comprovaram a atividade dessa substância sobre as duas formas evolutivas do parasito,

assim como sua baixa toxicidade. Além disso, promastigotas tratadas por 24 h com A3K2A3 nas concentrações de 3.4 e 9.3 μM (correspondentes às concentrações de IC_{50} e IC_{90} , respectivamente) foram utilizadas para a avaliação do possível mecanismo de ação dessa substância. Inicialmente, por meio de técnicas de microscopia eletrônica de transmissão, alterações ultraestruturais foram observadas, revelando principalmente danos mitocondriais e no núcleo, bem como acúmulo de corpos lipídicos. Adicionalmente, técnicas envolvendo fluorimetria e citometria de fluxo foram utilizadas para investigar as causas dessas alterações. Os resultados obtidos sugerem que o efeito antileishmania de A3K2A3 provocou morte celular via apoptose que foi inicialmente causada por um aumento nos níveis de espécies reativas de oxigênio dentro das células. Este aumento foi provavelmente responsável pelo colapso do potencial da membrana mitocondrial e pela redução dos níveis de ATP. O tratamento com A3K2A3 também desencadeou a externalização da fosfatidilserina, diminuição do volume celular, ativação de caspases, indução da fragmentação do DNA, alterações compatíveis com a morte celular por apoptose. A segunda parte desse estudo foi o desenvolvimento dos nanogéis a base de ácido hialurônico (AH). Para isso, cadeias de copolímeros termorresponsíveis, poli(DAAM-co-DMA), contendo grupos reticuláveis foram grafadas na cadeia de AH por química de tiol-eno. O derivado de AH obtido foi caracterizado por ressonância magnética nuclear de hidrogênio, permitindo confirmar a reação de acoplamento e determinar a quantidade de cadeias de copolímero grafadas no polissacarídeo. Verificou-se que o produto AH-m-poli(DAAM-co-DMA), quando aquecido acima de 32 °C foi capaz de se autoassociar formando nanogéis esféricos com um diâmetro em torno de 150 nm e um índice de polidispersão de 0,1. Este processo, porém, é reversível quando se diminui a temperatura abaixo da LCST (temperatura crítica da solução) do copolímero (LCST = 24 °C). Em seguida, a fim de obter nanogéis mais estáveis, estes foram submetidos a uma reação de reticulação utilizando o ácido isofitálico diidrazida (IDH). Este foi adicionado a uma solução de nanogéis a 40 °C, em condições fisiológicas e a reação entre os grupos ceto-funcionais do copolímero e a diidrazida bifuncional ocorreu espontaneamente por aproximadamente 24 h. Três concentrações de IDH foram utilizadas (0.5, 1.0 e 1.5 equivalentes molares) para garantir a eficiência da reticulação. Após reação de reticulação, a estrutura dos nanogéis tornou-se estabilizada por meio das ligações hidrazonas formadas, mesmo em baixa temperatura. Nanogéis não reticulados e reticulados foram então caracterizados por

meio de diferentes técnicas a fim de verificar tamanho, forma e confirmar as reações de reticulação realizadas por meio de técnicas de espalhamento de luz (DLS), microscopia eletrônica de varredura e criomicroscopia eletrônica. Nanogéis não reticulados e reticulados foram ainda utilizados para encapsular moléculas hidrofóbicas ativas, como o paclitaxel (agente anticancer). Foram também avaliadas a citotoxicidade em células tumorais (*in vitro*) e a biodistribuição dos nanogéis reticulados em um modelo tumoral xenográfico (TSA-pc). Os nanogéis apresentaram uma boa biocompatibilidade, e foram capturados por células tumorais. Além disso, foram capazes de circular por até 48 h no corpo do animal e ainda de se acumular no local do tumor.

CONCLUSÃO: A substância A3K2A3 induziu a morte celular nos protozoários tratados via disfunção mitocondrial, exibindo várias características indicativas de apoptose, incluindo o aumento de espécies reativas de oxigênio, despolarização mitocondrial, aumento na exposição de fosfatidilserina, redução do volume celular, e fragmentação do DNA. O estudo das principais vias envolvidas na morte dos protozoários fornece informações valiosas para o desenvolvimento de novas estratégias quimioterápicas. Além disso, nanogéis foram sintetizados a partir do AH modificado e puderam ser obtidos facilmente por auto associação desencadeada por temperatura, tendo sua estabilidade em meio fisiológico aumentada pela reticulação dos nanodomínios hidrofóbicos das cadeias de copolímero. A reticulação não afetou a eficiência de encapsulação das partículas e as propriedades biocompatíveis inerentes ao AH. Estes resultados sugerem que esses nanogéis possuem grande potencial como nanocarreadores de moléculas bioativas sendo promissores para o tratamento do câncer bem como de outras doenças infecciosas como as leishmanioses.

Palavras chaves: *Leishmania amazonensis*, leishmaniose, morte celular, apoptose, nanogéis termossensíveis, *crosslinking*, *drug-delivery*.

GENERAL ABSTRACT

INTRODUCTION AND OBJECTIVES: Leishmaniasis is a complex of diseases with important clinical spectrum and epidemiological diversity, representing a serious public health problem worldwide. Because it is a neglected disease, despite progress in fundamental knowledge about the parasite, current treatment against leishmaniasis is still unsatisfactory due to limited efficacy, increased cases of resistance, in addition to long treatment time and side effects. Thus, considering the antileishmanial potential already described for chalcone derivatives, the substance (1E, 4E) -2-methyl-1,5-bis (4-nitrophenyl) penta-1,4-dien-3-one (A3K2A3) presented as a promising candidate in preliminary *in vitro* tests. In this context, we have developed a detailed study of this activity, as well as its possible mechanism of action associated with parasite cell death. However, this chalcone derivative, as well as a considerable part of the new substances, presents high hydrophobicity, which is usually associated with several problems of *in vivo* administration, such as low absorption and systemic bioavailability, intravenous aggregation, among other effects, being able to limit its biological potential. Thus, in order to obtain a better result in the treatment of infectious diseases, it is necessary not only to investigate new compounds that possess therapeutic potential, but also to incorporate them into new technologies, such as nanoparticles, which allow an increase in biological activity, greater bioavailability and stability in physiological conditions, besides reducing possible side effects and a better therapeutic approach to patients. In this context, the objective of this work was to perform an *in vitro* study to understand the activity and mechanism of action of A3K2A3 involved in the cell death of these parasites as well as the development of nanogels based on hyaluronic acid as carriers of hydrophobic substances for target cells.

METHODS, RESULTS AND DISCUSSION: Initially, studies of the activity of A3K2A3 on promastigotes and intracellular amastigotes of *Leishmania amazonensis* and their cytotoxicity on red blood cells were performed. Results have confirmed the activity of this substance on the two evolutionary forms, as well as its low toxicity. In addition, promastigotes treated for 24 h with substance A3K2A3 at concentrations of 3.4 and 9.3 μM (corresponding to the concentrations of IC_{50} and IC_{90} , respectively) were used to evaluate the possible mechanism of action of this substance. Initially, by

means of transmission electron microscopy techniques, ultrastructural alterations were found, mainly revealing mitochondrial and nucleus damages, as well as accumulation of lipid bodies. In addition, techniques based on fluorimetry and flow cytometry were used to investigate the causes of these changes. The results obtained suggest that the antileishmanial effect of A3K2A3 caused cell death via apoptosis which was initially caused by an increase in the levels of reactive oxygen species within the cells. This increase was probably responsible for the collapse of mitochondrial membrane potential and the reduction of ATP levels. Treatment with A3K2A3 also triggered the externalization of phosphatidylserine, decreased cell volume, activation of caspases and DNA fragmentation, which are changes compatible with cell death through apoptosis. The second part of this study was the development of nanogels based on hyaluronic acid (HA). To this end, thermo-responsive poly(DAAM-co-DMA) copolymer chains containing crosslinkable groups were grafted on the HA chain by thiol-ene chemistry. The obtained HA derivative was characterized by ^1H NMR, allowing to confirm the coupling reaction and to determine the amount of copolymer that were grafted on the polysaccharide. The HA-m-poly(DAAM-co-DMA), when heated above 32°C , was able to self-assemble into spherical nanogels with a diameter around 150 nm and a polydispersity index of 0.1. This process, however, is reversible when the temperature decreases below the LCST (lower critical solution temperature) of the copolymer (LCST = 24°C). Then, in order to obtain stabilized nanogels, they were subjected to a cross-linking reaction using isophthalic acid dihydrazide (IDH). It was added to a solution of nanogels at 40°C under physiological conditions and the reaction between the keto-functional groups of the copolymer and the bifunctional dihydrazide occurred spontaneously for approximately 24 h. Three concentrations of IDH were used (0.5, 1.0 and 1.5 molar equivalents) to ensure crosslinking efficiency. After core cross-linking reaction, the structure of the nanogels became stabilized through the formed hydrazone bonds, even at low temperature. Non-crosslinked and crosslinked nanogels were then characterized by different techniques (light scattering, scanning electron microscopy and electronic cryoscopy) in order to verify size, shape and to confirm the crosslinking reaction. Non-crosslinked and crosslinked nanogels were further used to encapsulate active hydrophobic molecule, such as paclitaxel (anticancer agent). Cytotoxicity in tumor cells (*in vitro*) and biodistribution of the crosslinked nanogels in a xenograft tumor model (TSA-pc) were also evaluated. The nanogels showed good

biocompatibility, and were captured by tumor cells. In addition, they were able to circulate up to 48 h in mice body and still accumulate in the tumor site.

CONCLUSION: A3K2A3 induced cell death in protozoa treated through mitochondrial dysfunction, exhibiting several characteristics indicative of apoptosis, including increased reactive oxygen species, mitochondrial depolarization, increased phosphatidylserine exposure, reduced cell volume, and DNA fragmentation. The study of the main pathways involved in the death of protozoa provides valuable information for the development of new chemotherapeutic strategies. In addition, nanogels were synthesized from hyaluronic acid modified with a ketone-functional copolymer and could be easily obtained by self-assembling triggered by temperature, with enhanced stability in physiological conditions through the core cross-linking of the hydrophobic nanodomains of the copolymer chains. Crosslinking did not affect either the encapsulation efficiency of the particles and the biocompatible properties inherent to HA. These results suggest that these nanogels have great potential as nanocarriers of bioactive molecules being promising for the treatment of cancer as well as for other infectious diseases such as leishmaniasis.

Keywords: *Leishmania amazonensis*, leishmaniasis, cell death, apoptosis, thermosensitive nanogels, crosslinking, drug-delivery.

SUMÁRIO

ARTIGO 1: “A3K2A3-induced Apoptotic Cell Death of <i>Leishmania amazonensis</i> Occurs Through Caspase- and ATP-dependent Mitochondrial Dysfunction”.....	12
1.Introduction	14
2. Materials and Methods	15
3. Results	21
4. Discussion	24
5. Conclusion	28
6. References	29
7. Figures	37
ARTIGO 2: “Tuning the stability of self-assembled nanogels based on hyaluronic acid using ketone-hydrazide cross-linking”.....	49
1. Introduction	51
2. Materials and Methods	55
3. Results and discussion	59
4. Conclusion	65
5. References	67
6. Figures	70

Artigo 1

A3K2A3-induced Apoptotic Cell Death of *Leishmania amazonensis* Occurs Through Caspase- and ATP-dependent Mitochondrial Dysfunction

Francielle Pelegrin Garcia¹, Jean Henrique da Silva Rodrigues¹, Zia Ud Din², Edson Rodrigues-Filho², Tânia Ueda-Nakamura¹, Rachel Auzély-Velty³, Celso Vataru Nakamura^{1*}.

¹*Laboratório de Inovação Tecnológica no Desenvolvimento de Fármacos e Cosméticos, Universidade Estadual de Maringá, Av. Colombo 5790, 87020-900, Bloco B-08 Maringá, PR, Brazil*

²*LaBioMMi, Departamento de Química, Universidade Federal de São Carlos, CP 676, 13.565-905 São Carlos, SP, Brazil*

³*Université Grenoble Alpes, CERMAV; CNRS, F-38000 Grenoble, France*

* Corresponding author: Celso Vataru Nakamura, Programa de Pós-graduação em Ciências Biológicas, Laboratório de Inovação Tecnológica no Desenvolvimento de Fármacos e Cosméticos, Bloco B-08, Universidade Estadual de Maringá, Av. Colombo 5790, CEP 87020-900, Maringá, Paraná, Brazil. Phone number: +55 44 3011-5012, Fax: +55 44 3011-5046. E-mail address: cvnakamura@uem.br

ACKNOWLEDGMENTS

This work was supported through grants from the Conselho Nacional de Desenvolvimento Científico e Tecnológico – CNPq, Capacitação de Aperfeiçoamento de Pessoal de Nível Superior – CAPES, Financiadora de Estudos e Projetos – FINEP, Programa de Pós-Graduação em Ciências Biológicas da Universidade Estadual de Maringá and Complexo de Centrais de Apoio a Pesquisa COMCAP – UEM

ABSTRACT

Leishmaniasis is a neglected tropical disease that affects millions of people worldwide. Current therapies mainly rely on antimonial drugs that are inadequate because of their high toxicity and increased drug resistance. An urgent need exists to discover new, more effective, more affordable, and more target-specific drugs. Pathways that are associated with apoptosis-like cell death have been identified in unicellular eukaryotes, including protozoan parasites. In the present study, we studied the mechanism of cell death that is induced by A3K2A3 against *L. amazonensis*. A3K2A3 is a dibenzylideneacetone that has an acyclic dienone that is attached to aryl groups in both β -positions, which is similar to curcuminoids and chalcone structures. This compound was previously shown to be safe with regard to cytotoxicity and active against the parasite. Biochemical and morphological approaches were used in the present study. The results suggested that A3K2A3 caused mitochondrial dysfunction in *L. amazonensis* promastigotes, leading to mechanisms of cell death that share some common phenotypic features with metazoan apoptosis, such as an increase in reactive oxygen species production, a decrease in the adenosine triphosphate ratio, phosphatidylserine exposure, a decrease in cell volume, caspase production, and DNA fragmentation. Altogether, these findings indicate that apoptosis can indeed be triggered by chemotherapeutic agents.

Keywords: *Leishmania amazonensis*, dibenzylideneacetone, mitochondria, cell death, apoptosis.

1. INTRODUCTION

Leishmaniasis remains endemic in several parts of the world and is a serious health problem in numerous developing countries. It occurs as a complex and clinically diverse illness that is caused by protozoan *Leishmania* species that are transmitted through the bite of sandflies. Despite recent advances, the treatment of leishmaniasis is still problematic because of the high toxicity and adverse side effects of therapeutic drugs. The need to identify new molecular targets to improve therapy is clearly justified. Target-identification and mechanism-of-action studies play important roles in drug discovery. The putative target should be either absent in the host or markedly different from the host homolog so that it can be exploited as a drug target [1].

Interestingly, programmed cell death in protists appears to share some morphological features with apoptosis in multicellular organisms, including cell shrinkage, the loss of mitochondrial membrane potential, and the externalization of phosphatidylserine [2,3]. A better understanding of the mechanistic machinery of apoptosis-like programmed cell death in protists would thus prove immensely beneficial in the design of rational chemotherapeutic interventions in a target-dependent manner [4].

1,5-Diarylpentanoid dibenzylideneacetone is the parent compound of a class of compounds that have an acyclic dienone that is attached to aryl groups in both β -positions. These structures resemble those of curcuminoids (1,7-diarylheptanes) and chalcones (1,3-diarylpropanes), which are very important bioactive natural compounds that are found in many plant species [5]. Dibenzylideneacetones (DBAs) and their analogues have antiproliferative, antiinflammatory, and apoptotic effects through the regulation of multiple signaling pathways in cancer cell lines [6-10]. Dibenzylideneacetone has been reported to enhance TRAIL-induced (cytokine tumor necrosis factor (TNF)-related apoptosis-inducing ligand) apoptosis by regulating cell-survival proteins and pro-apoptotic proteins through the activation of reactive oxygen species (ROS) and CHOP (C/EBP homologous protein) in colon cancer cells [11]. The good bioavailability of some dibenzylideneacetones and their derivatives, which is required for bioactivity, and their mode of cross linking have raised chemists' interest in their synthesis [5].

Our previous study reported the anti-leishmanial and anti-trypanosomal effects of A3K2A3 (2d) [5]. Considering its anti-leishmanial activity and selectivity for parasites, the aim of the present study was to better characterize the biochemical alterations that are induced by this compound against promastigote forms of *L. amazonensis* and elucidate the possible mechanism of action of A3K2A3 that is involved in the cell death of this protozoan.

2. MATERIALS AND METHODS

2.1 Chemicals

Actinomycin D, antimycin A, bovine serum albumin, carbonyl cyanide m-chlorophenylhydrazone (CCCP), digitonin, dimethylsulfoxide (DMSO), rhodamine 123 (Rh123), 2',7'-dichlorofluorescein diacetate (H₂DCFDA), Nile Red, and 4,5-diaminofluorescein (DAF-2) were purchased from Sigma-Aldrich (St. Louis, MO, USA). Fetal bovine serum (FBS) was obtained from Invitrogen (Grand Island, NY, USA). Annexin-V FITC, 3,8-phenanthridinediamine-5-(6-triphenylphosphoniumhexyl)-5,6-dihydro-6-phenyl (MitoSOX), and propidium iodide (PI) were obtained from Invitrogen (Eugene, OR, USA). Diphenyl-1-pyrenylphosphine (DPPP), the APO-BrdU terminal deoxynucleotidyl transferase enzyme mediated dUTP end labeling (TUNEL) Assay Kit, and the EnzChek Caspase-3 Assay Kit were purchased from Molecular Probes (Eugene, Oregon, USA). CellTiter-Glo was obtained from Promega (Madison, WI, USA). All of the other reagents were of analytical grade.

2.1. Synthesis and preparation of A3K2A3

A3K2A3 was synthesized as previously described by Ud Din et al. [5]. Stock solutions were aseptically prepared in DMSO and diluted in culture medium so that the DMSO concentration did not exceed 1% in the experiments. The concentrations of A3K2A3 that were used in the assays were 3.4 and 9.3 μ M, representing the IC₅₀ and IC₉₀, respectively, as described previously [5].

2.2. Parasites

Leishmania amazonensis promastigotes (MHOM/BR/Josefa) were maintained at 25°C in Warren's medium (brain-heart infusion plus hemin and folic acid; pH 7.2) supplemented with 10% heat-inactivated FBS.

2.3. *In vitro* antiproliferative assay

Promastigotes in the logarithmic phase (1×10^6 parasites/ml) were grown in 24-well culture microplates at 25°C in Warren's medium supplemented with 10% FBS. Parasites were then incubated in the presence of different concentrations of A3K2A3 (1-100 μ M). Anti-leishmanial activity was determined by directly counting free-living parasites in a Neubauer chamber daily until 72 h of incubation, and the concentration vs. percentage of growth inhibition was plotted each day, in order to determine the inhibition concentration of 50% of parasites (IC_{50}).

2.4. Activity against intracellular amastigotes

Peritoneal macrophages were collected from BALB/c mice by washing with cold phosphate-buffered saline (PBS) supplemented with 3% FBS. The animal protocol was approved by the Ethical Committee of the State University of Maringá (approval no. 029/2014). Sterile glass coverslips were placed in the wells of a 24-well microplate, and 5×10^5 cells/ml were added to each well in RPMI 1640 medium supplemented with 10% FBS. The microplate was incubated for 2 h at 37°C in a 5% CO₂-air mixture to adhere macrophages. The macrophage monolayer was infected with promastigote forms at a 7:1 (parasite: macrophage) ratio. After 4 h of interaction at 34°C in a 5% CO₂-air mixture, the microplate was washed with RPMI 1640 medium to remove non-interiorized parasites. Afterward, the infected macrophages were treated with A3K2A3 at different concentrations (1, 2.5, 5.0, and 10 μ M) and incubated for 48 h. The percentage of infected macrophages was evaluated after Giemsa staining by microscopically counting the number of amastigotes per macrophage [12].

2.5. Hemolytic activity

Another way to assess the safety of a drug is to measure its hemolytic activity. Defibrinated sheep blood was washed in glycosylated saline to remove any free hemoglobin from the defibrination process. Red blood cells were inoculated in 96-well plates at 3% in glycosylated saline with different concentrations of A3K2A3 (10-

2000 μM). The plates were incubated for 3 h at 37°C, and the supernatant was read at 550 nm. To calculate the percentage of hemolysis, 1% Triton X-100 was used as a positive control [13].

2.6. Transmission electron microscopy

For the ultrastructural analysis, promastigote forms were treated for 72 h at 25°C with concentrations of A3K2A3 that corresponded to the IC₅₀ and IC₉₀. After washing with PBS, the parasites were fixed in 2.5% glutaraldehyde in 0.1 M sodium cacodylate buffer at 4°C and post-fixed in a solution that contained 1% osmium tetroxide, 0.8% potassium ferrocyanide, and 5 mM calcium chloride. The parasites were dehydrated in an acetone series and embedded in Epon resin for 72 h at 60°C. Ultrathin sections were stained with 5% uranyl acetate and lead citrate and examined in a JEOL JEM 1400 transmission electron microscope.

2.7. Detection of cytoplasmic lipid bodies by Nile Red staining

Promastigote forms of *L. amazonensis* were treated with concentrations of A3K2A3 that corresponded to the IC₅₀ and IC₉₀ as described previously in the antiproliferative assay. The treated parasites were then harvested, washed twice in PBS, and directly stained with 10 $\mu\text{g/ml}$ Nile Red (Sigma-Aldrich, St. Louis, MO, USA) for 30 min at room temperature. Cytoplasmic lipid bodies in the parasites were detected with an epifluorescence microscope (Olympus BX51) equipped with a WG filter. Parasites were photographed using an Olympus UC30 camera. The samples were also analyzed in a fluorescence microplate reader (Victor X3, PerkinElmer, Finland) at an excitation wavelength of 515-560 nm and emission wavelength > 590 nm.

2.8. Determination of mitochondrial transmembrane potential ($\Delta\Psi\text{m}$)

Promastigotes (1×10^7 cells/ml) were treated with 3.4 and 9.3 μM A3K2A3 for 24 h at 37°C, harvested, and washed with PBS. The parasites were incubated with 1 ml (5 mg/ml in ethanol) of Rh123, a fluorescent probe that accumulates in mitochondria, for 15 min, resuspended in 0.5 ml PBS, and incubated for an additional 30 min. The assay was conducted according to the manufacturer's instructions. The parasites were analyzed using a BD FACSCalibur flow cytometer and CellQuest Pro software (Becton Dickinson; Franklin Lakes, NJ, USA). A total of 10,000 events were acquired in the

region that corresponded to the parasites. CCCP (100 μM) was used as a positive control [14].

2.9. Measurement of reactive oxygen species

Promastigotes (1×10^7 cells/ml) were treated or untreated with 3.4 and 9.3 μM A3K2A3 for 24 h, centrifuged, washed, and resuspended in PBS, pH 7.4. Afterward, these parasites were loaded with 10 μM of the permeant probe H₂DCFDA in the dark for 45 min [15]. Reactive oxygen species were measured as an increase in fluorescence that is caused by the conversion of the nonfluorescent dye to highly fluorescent 20,70-dichlorofluorescein. Parasites were analyzed using a BD ACCURI™ C6 flow cytometer with a total of 10,000 events acquired in the pre-determined region that corresponded to the parasites. Additionally, fluorescence was also measured in a microplate reader (Victor X3, PerkinElmer, Finland) at an excitation wavelength of 488 nm and emission wavelength of 530 nm. Hydrogen peroxide (20 mM) was used as a positive control.

2.10. Estimation of lipid peroxidation by diphenyl-1-pyrenylphosphine assay

Promastigote forms of *L. amazonensis* (1×10^6 cells/ml) were treated with 3.4 and 9.3 μM A3K2A3 for 24 h at 25°C. The cells were washed twice, resuspended in PBS, and loaded with DPPP [16] for 15 min. During the labeling procedure, the cell suspension was kept in the dark. After incubation, fluorescence intensities of the samples were measured with a fluorescence microplate reader (Victor X3, PerkinElmer, Finland) at an excitation wavelength of 355 nm and emission wavelength of 460 nm. Hydrogen peroxide (200 μM) was used as a positive control.

2.11. Intracellular adenosine triphosphate determination

Promastigotes of *L. amazonensis* (1×10^6 cells/ml) were treated with 3.4 and 9.3 μM A3K2A3 for 24 h. After incubation at 25°C, the promastigotes were centrifuged, washed, and resuspended in PBS. In white 96-well plates, equal volumes of CellTiter-Glo reagent and an aliquot of each sample were added, mixed, and incubated for 10 min. The luminescence intensity was quantified using a luminescence microplate reader (VICTOR X3, PerkinElmer). CCCP (100 μM) was used as a positive control.

2.12. Determination of cellular membrane integrity

Promastigotes (1×10^7 cells/ml) were treated with 3.4 and 9.3 μM A3K2A3 for 24 h at 32°C, harvested, and washed with PBS. The parasites were incubated with 50 μl of 2 mg/ml Propidium iodide (PI) for 5 min according to the manufacturer's instructions. Immediately thereafter, the parasites were analyzed using a BD FACSCalibur flow cytometer equipped with CellQuest software. A total of 10,000 events were acquired in the region that corresponded to the parasites. Digitonin (40.0 μM) was used as a positive control [17].

2.13. Promastigotes and intracellular amastigotes scanning electron microscopy

Promastigotes (1×10^6 cells/ml) and peritoneal macrophages adhered to the surface of small glass coverslips previously infected with promastigotes for 4 h at 34°C (as described in 2.4. item) were prepared. After the infection period plates were incubated at 34 °C for 24 h, and just then cells were treated with 3.4 and 9.3 μM A3K2A3 for 48 h and 24 h at the same temperature, in order to assess the morphological alterations in promastigotes and intracellular amastigotes, respectively. After treatment cells were fixed in 2.5% glutaraldehyde in 0.1 M sodium cacodylate buffer for 1-3 h. Subsequently, they were dehydrated in increasing concentrations of ethanol and critical-point dried in CO_2 . For intracellular amastigotes observation, the slides were placed in an appropriate apparatus and infected macrophages were fractured with adhesive tape. All samples were coated with gold, and observed in a Shimadzu SS-550 (Japan) scanning electron microscope [18, 19].

2.14. Determination of cell volume of parasites

Promastigotes (1×10^7 cells/ml) were treated with 3.4 and 9.3 μM A3K2A3 for 24 h at 25°C, harvested, and washed with PBS. Subsequently, the parasites were analyzed using a BD FACSCalibur flow cytometer and CellQuest Pro software. Histograms were generated, and FSC-H represented the cell volume. A total of 10,000 events were acquired in the region that corresponded to the parasites. Actinomycin D (20.0 mM) was used as a positive control [18].

2.15. Determination of phosphatidylserine exposure

Promastigotes (1×10^6 cells/ml) were treated with 3.4 and 9.3 A3K2A3 for 24 h at 25°C. Afterward, the parasites were washed and resuspended in 100 μl of binding buffer

(140 mM NaCl, 5 mM CaCl₂, and 10 mM HEPES-Na, pH 7.4), followed by the addition of 5 µl of the calcium-dependent phospholipid binding protein annexin-V FITC for 15 min at room temperature. Binding buffer (400 µl) was then added. Antimycin A (125.0 µM) was used as a positive control. Data acquisition was performed using a fluorescence microplate reader (Victor X3, PerkinElmer, Finland) at an excitation wavelength of 488 nm and emission wavelength of 520 nm. Additionally, cells were counterstained with PI (0.2 µg/mL) and images were acquired by an epifluorescence microscope (Olympus BX51) using an Olympus UC30 camera. Cells that were stained with annexin-V were considered apoptotic [20].

2.16. Caspase detection

Caspase-3/7 protease activity was measured using the EnzChek Caspase-3 Assay Kit (Molecular Probes). The assay was performed according to the manufacturer's instructions with the following minor modifications. Briefly, 10⁶ parasites were incubated with 3.4 and 9.3 µM A3K2A3 for 24 h, washed, and lysed with Triton X-100 in 1% PBS for 30 min, followed by the addition of kit reagents (i.e., reaction buffer, dithiothreitol, and 5 mM Z-DEVD-AMC substrate) and incubation for 30 min. When the reactions were completed, the increase in fluorescence, which is indicative of cleavage of the Z-DEVD-AMC substrate, was fluorometrically read at excitation and emission wavelengths of 342 and 441 nm, respectively. The reactions were performed with and without the Ac-DEVD-CHO inhibitor (1 mM). Camptothecin (20 µM) was used as a positive control.

2.17. Determination of DNA fragmentation

In addition to determine DNA fragmentation and nuclease activity, promastigote forms of *L. amazonensis* (1 × 10⁷ cells/ml) were treated with 3.4 and 9.3 µM A3K2A3 for 24 h at 25°C. Treated cells were fixed with 4% paraformaldehyde and incubated with 0.2% Triton X-100 for 10 min for permeabilization and then layered with a TdT reaction mixture that contained BrdUTP for 2 h at 37°C according to the manufacturer's instructions with minor modifications (APO-BrdU TUNEL Assay Kit, with Alexa Fluor 488 Anti-BrdU). Cells that were linked with BrdU were detected using a green-fluorescent Alexa Fluor 488 dye-labeled anti-BrdU antibody for 30 min. Fluorescence was fluorometrically quantified in a microplate reader at an excitation wavelength of

485 nm and emission wavelength of 520 nm. Camptothecin (10 μM) was used as a positive control.

2.18. Statistical analysis

The data that are presented in the graphs are expressed as the mean \pm standard deviation (SD) of at least three independent experiments. The data were analyzed using one- and two-way analysis of variance (ANOVA). Significant differences among means were identified using the Tukey or Bonferroni *post hoc* test. Values of $p \leq 0.05$ were considered statistically significant. The statistical analyses were performed using Prism 5 software (GraphPad, San Diego, CA, USA).

3. RESULTS

In a previous study, A3K2A3 presented interesting activity against promastigotes of *L. amazonensis*, with an IC_{50} of $3.4 \pm 0.07 \mu\text{M}$, demonstrating its effects against this protozoan parasite (Ud Din *et al.*, 2014). In the present study, we further investigated this activity and mechanism of action.

To confirm the previously reported effects of A3K2A3 (Fig. 1) on the cellular proliferation of *L. amazonensis*, daily parasite counts were performed, and growth inhibition curves were constructed for each day of the experiment. A3K2A3 inhibited the growth of promastigotes at a similar IC_{50} ($2.6 \pm 0.3 \mu\text{M}$) after 72 h of treatment. Interestingly, with 24 h incubation, A3K2A3 had an IC_{50} of $2.7 \pm 0.7 \mu\text{M}$, indicating potent activity even after only a few hours of incubation (Fig. 2). For intracellular amastigotes, A3K2A3 also presented potent activity, with an IC_{50} of $2.9 \pm 0.5 \mu\text{M}$.

The cytotoxicity effects of A3K2A3 on J774A1 macrophages were tested as described previously ($\text{CC}_{50} = 43.0 \pm 4.24 \mu\text{M}$). To corroborate its non-cytotoxic profile, the hemolytic activity of this substance was assayed. A3K2A3 up to a concentration of 2,000 μM did not present hemolytic activity. The percentage of hemolysis was less than 6% (data not shown).

To further investigate and identify the organelles that might be potential targets of A3K2A3 in promastigotes, transmission electron microscopy (TEM) was performed as described previously. A3K2A3 caused significant ultrastructural alterations (Fig. 3), including the disorganization of Golgi complex (disintegration of the stacks of cisternae

and formation of clusters of tubules and vesicles dispersed in the cytoplasm) and nuclei and accumulation of cytoplasmic lipid bodies. A3K2A23 also caused severe damage in parasite mitochondria, reflected by extensive swelling and disorganization of the inner mitochondrial membrane, intense cytoplasmic vacuolization, and the presence of concentric membrane structures inside the organelle. These changes were observed in greater proportions when the cells were treated with the IC₉₀ of A3K2A3. Control parasites had an apparently normal ultrastructure (Fig. 3A).

To confirm the accumulation of lipid bodies in treated promastigotes that was observed by TEM, we evaluated the existence of this structure by Nile Red staining, which stains neutral lipids. Fluorescence microscopy revealed an increase in the presence of lipid bodies in promastigotes after treatment with the IC₅₀ and IC₉₀ of A3K2A3 for 24 h (Fig. 4) compared with non-treated cells. This finding was confirmed by fluorimetry, with a 2.7-fold increase in fluorescence in cells that were treated with the IC₉₀ of A3K2A3 compared with control cells (i.e., without treatment).

Transmission electron microscopy also revealed a pronounced effect of A3K2A3 on *L. amazonensis* mitochondria. Therefore, the $\Delta\Psi_m$ was evaluated by flow cytometry in treated parasites. Histograms showed a marked decrease in total Rh123 fluorescence intensity in promastigotes after 24 h treatment at all of the concentrations tested compared with the control group, indicating mitochondrial depolarization (Fig. 5). This loss of $\Delta\Psi_m$ was higher at the IC₉₀ (40.11%) than at the IC₅₀ (27.00%). The positive control, CCCP, induced a 72.96% decrease in $\Delta\Psi_m$.

Given the $\Delta\Psi_m$ results, to investigate possible oxidative damage that is caused by A3K2A3 in promastigotes, the production of total ROS was investigated using the fluorescent probe H₂DCFDA, which primarily detects H₂O₂ and hydroxyl radicals [21]. A3K2A3 increased total ROS production at all of the concentrations tested compared with the control group (Fig. 6A), with 45.87% and 12.00% increases at the IC₅₀ and IC₉₀ of A3K2A3, respectively. The positive control (H₂O₂) increased the fluorescence intensity by 89.74%. These results were also confirmed by flow cytometry analysis (Fig. 6B), by which it was possible to identify that at a populational level, 93.8% and 98.9% of the analyzed cells presents some evidence of oxidative stress after IC₅₀ and IC₉₀ treatment, respectively, against only 3.98% of positivity at untreated populations.

Our previous experiment showed that A3K2A3 caused mitochondrial damage and oxidative imbalance in *L. amazonensis*, leading to enhanced ROS production. Thus,

we expected that A3K2A3 may trigger molecular and structural alterations in the parasite through oxidative reactions. Lipid peroxidation was assessed by measuring total fluorescent lipid peroxidation products in leishmanial cells after treatment with A3K2A3 using DPPP, which stoichiometrically reacts with lipid hydroperoxides to yield the fluorescent product DPPP oxide. A3K2A3 treatment significantly increased lipid peroxides after 24 h of treatment at both concentrations tested (Fig. 7).

Because the disruption of mitochondrion function translates into a reduction of ATP generation, the levels of ATP were measured after exposure to A3K2A3, using CellTiter-Glo reagent, which is detected by luminescence. A gradual decrease in ATP levels was observed as the A3K2A3 concentration increased after 24 h of treatment (Fig. 8).

To determine the possible mechanism of cell death that is triggered by A3K2A3, alterations in cell membrane integrity were evaluated using PI staining. A3K2A3-treated, PI-labeled promastigotes did not exhibit significant permeabilization of the plasma membrane compared with untreated parasites. A3K2A3 at concentrations of 3.4 and 9.3 μM showed 4.75% and 6.16%, respectively, of the cells PI-positive. The negative control showed a PI fluorescence intensity of 4.15%, and digitonine (i.e., the positive control) showed a PI fluorescence intensity of 57.12% (data not shown).

Scanning electron microscopy of promastigotes was used to investigate the mechanism of cell death by identifying morphological alterations that were induced by A3K2A3 in the parasite. The photomicrographs showed that untreated protozoa exhibited typical characteristics, with an elongated shape and terminal flagellum. In contrast, A3K2A3 dose-dependently altered the size and shape of the parasites, including a rounding and overall reduction of the cell body (Fig. 9). Alterations were also observed in intracellular amastigote forms treated with both concentrations of A3K2A3 in scanning electron microscopy: damage and disruption to the amastigotes cell membrane and a reduction in amastigotes number per cell (Fig. 10).

Additional experiments were performed to evaluate cell shrinkage, a hallmark of apoptotic death. As shown in Figure 11, a decrease in cell volume was observed in cells that were treated with 3.4 and 9.3 μM A3K2A3 after 24 h and analyzed by flow cytometry, with reductions of 22.26% and 27.66%, respectively. The positive control, actinomycin D, decreased cell volume by 47.20%.

To determine whether the mechanism of cell death that is triggered by A3K2A3 involves apoptosis, we evaluated the externalization of phosphatidylserine, an apoptotic marker that is present in the outer leaflet of plasmalemma [22], in promastigotes that were treated with A3K2A3 for 24 h and stained with FITC-conjugated annexin-V. As shown in Fig. 12, A3K2A3 increased the annexin-V fluorescence intensity more than 8 times at both the IC₅₀ and IC₉₀ compared with the negative control group, indicating phosphatidylserine exposure. Moreover, fluorescence microscopy revealed parasites labeled by annexin-V-FITC after treatment with both concentrations of A3K2A3 (3.4 and 9.3 μM). At the higher concentration (9.3 μM) of drug tested, it is also possible to identify some PI staining at the nucleus, indicating some compromise of cell membrane integrity, probably due to a later apoptotic process.

A major feature of apoptotic death is the involvement of cysteine aspartate proteases (caspases) that mediate events downstream of the mitochondria, most notably the executioners caspase 3 and 7 [23, 24]. To further substantiate the existence of these proteases in *L. amazonensis*, a fluorometric assay using EnzChek Caspase-3 Assay Kit was performed. The substrate DEVD-AFC was added to this extract, and the release of AFC was used as a measure of mature caspase-3-like protease activity in A3K2A3-treated cells. A significant increase in these proteases was observed after treatment with A3K2A3 for 24 h compared with untreated cells. This effect was more pronounced in promastigotes treated with the IC₉₀ (Fig. 13).

The TUNEL assay detects apoptosis at the single-cell level and thus permits a better evaluation of the apoptotic cell fraction [22]. As shown in Fig. 14, promastigotes that were treated with different concentrations of A3K2A3 and subjected to the TUNEL assay exhibited a significant increase in fluorescence intensity at both concentrations tested. The IC₅₀ (3.4 μM) promoted a > 2-fold increase in fluorescence compared with untreated parasites (i.e., the negative control), thus indicating DNA fragmentation. Camptothecin, the positive control, caused increase of more than 9-fold in fluorescence intensity.

4. DISCUSSION

Drug therapy for leishmaniasis has not significantly advanced since the beginning of the 20th century, and adequate treatment remains a problem. There

continues to be an urgent need to develop more rational and effective therapeutic drugs [25].

Dibenzylideneacetone derivatives are a class of substances that have an acyclic dienone that is attached to aryl groups in both β -positions, with a broad spectrum of biological activity, especially antitumor activity [11, 26]. A3K2A3 has been previously reported to have interesting anti-trypanosomal and anti-leishmanial activity, and it has been shown to be more selective to parasites than to mammalian and macrophage cells [5]. A better understanding of the mechanism of cell death would be helpful for developing therapeutic interventions against parasites. In the present study, we evaluated the anti-leishmanial activity of A3K2A3 to delineate its putative mechanism of action.

This compound at low micromolar concentrations presented significant activity against promastigote and intracellular amastigote forms of *L. amazonensis* and did not affect the viability of red blood cells. These results are very interesting because amastigote forms of *Leishmania* are responsible for clinical manifestations in the vertebrate host. These amastigotes are the major target of chemotherapy for leishmaniasis [27].

Unicellular kinetoplastid parasites have special organelles that are involved in essential metabolic pathways, with steps that differ from their mammalian counterparts, thus making them attractive targets for new chemotherapeutic agents. Ultrastructural studies can be very helpful for achieving this goal [28, 29]. To obtain information about the mechanism of action of A3K2A3 against *L. amazonensis*, promastigotes were analyzed by TEM. Photomicrographs of A3K2A3-treated cells exhibited important ultrastructural alterations, such as lipid body accumulation and Golgi complex disorganization. Extensive degradation of the Golgi complex and endoplasmic reticulum that is caused by the accumulation of intracellular lipid bodies in the cytoplasm, indicated by fluorescence microscopy and fluorimetry (Nile Red staining), may indicate alterations in phospholipids and sterol content and may also be related to exocytic activity and autophagy. Some studies have reported that this exocytic activity might occur as a result of the secretion of abnormal lipids into this region, which accumulate as a consequence of drug action or might indicate a process of exacerbated protein production by the cells [30-32].

Furthermore, ultrastructural analyses of the treated parasites revealed that the mitochondria was one of the most affected organelles, which could also be related to possible alterations in lipid composition. Therefore, we focused on investigating mitochondrial alterations and their consequences, especially with regard to parasite death. A3K2A3 may exert its anti-leishmanial activity by affecting mitochondrial function in the parasite, demonstrated by TEM, a decrease in $\Delta\Psi_m$, and an increase in mitochondrial ROS production.

Electrons move through the mitochondrial respiratory chain during oxidative phosphorylation, and a proton gradient is established across the inner mitochondrial membrane as an energy source for ATP. A decrease in Rh123 fluorescence intensity suggests an increase in proton permeability across the inner mitochondrial membrane, which can decrease ATP synthesis and result in parasite death [13, 33, 34], especially because the parasite depends mainly on oxidative phosphorylation for ATP production [35]. The depletion of ATP levels was observed after treating the promastigotes with A3K2A3. For organisms with a single mitochondria, such as *Leishmania*, there is no possibility of compensating the injured mitochondria. Therefore, survival depends on the proper functioning of a single organelle [36].

Our results are consistent with a previous study that reported that ATP levels gradually decreased after the loss of $\Delta\Psi_m$ during treatment with H_2O_2 [37]. Adenosine triphosphate is a key molecule for chromatin condensation, nuclear fragmentation and regulation, and the maintenance of ion homeostasis during apoptosis. Therefore, we can assume that ATP levels were generated prior to the loss of $\Delta\Psi_m$, and ATP that was supplied by glycolysis was sufficient to perform these cellular activities and propagate programmed cell death in leishmanial cells [38].

We also found a significant increase in ROS production after A3K2A3 treatment in promastigotes. Mitochondrial ROS formation is essential for various signaling processes and strongly involved in the degenerative process through damage to macromolecules, mainly proteins, lipids, and DNA [39-41]. Promastigotes that were treated with A3K2A3 exhibited an increase in the ratio of lipid peroxidation. Earlier studies found that Camptothecin induced the formation of ROS inside leishmanial cells and also increased the level of lipid peroxidation [22].

In multicellular and unicellular organisms, mitochondria serve as an important cellular source of ROS, which are critical for the induction of apoptosis. The production

of ROS during the early phase of apoptosis usually follows an imbalance in cellular redox homeostasis [42]. Indeed, previous studies have shown that antimony exerts its anti-leishmanial effect by generating ROS and depleting thiols within both parasites and macrophages [43-45].

A3K2A3 treatment also induced the externalization of phosphatidylserine, which was visualized by annexin-V staining. The translocation of phosphatidylserine from inside the plasma membrane to the outer layer is a common alteration that occurs during programmed cell death [46-48]. In addition to biochemical alterations, apoptosis also causes morphological alterations [49]. Based on this, we evaluated cell shrinkage (i.e., a hallmark of apoptotic death). Our SEM observations revealed swelling and overall rounding of A3K2A3-treated cells, which was also confirmed by flow cytometry. Membrane integrity was also evaluated, but it was not significantly altered by A3K2A3 treatment, reflected by a low ratio of PI staining. Therefore, we could exclude the possibility that necrosis was the main pathway of cell death.

The apoptotic process is associated with signaling cascades that involve mitochondria (intrinsic pathway) or death receptors (extrinsic pathway) [50]. Stimulation of the intrinsic mitochondrial apoptotic pathway by ROS and mitochondrial DNA damage promotes outer membrane permeabilization and the mitochondrion-to-cytosol translocation of cytochrome c, AIF (apoptosis-inducing factor), and Smac/Diablo, which trigger caspase-dependent or caspase-independent cytosolic signaling events [51].

Immediately after the loss of $\Delta\Psi_m$, protons are released into the cytosol from mitochondria, and this contributes to intracellular acidification in leishmanial cells, similar to mammalian cells [52]. Changes in pH modulate the apoptotic responsiveness of the cell and amplify the apoptotic program by regulating the activity of caspase-like proteases [36].

It is well known that caspases (i.e., a family of cysteine proteases) are involved in orchestrating apoptosis in metazoan. Caspase homologues known as metacaspases (MCAs) in *Trypanosoma* and *Leishmania* have been reported to play distinct roles in Programmed Cell Death [53, 54]. The role of MCAs is subject to debate: roles in cell cycle control, in cell death or even in cell survival have been suggested. It was shown, using a *Leishmania major* MCA-deficient strain, that *L. major* MCA (LmjMCA) not

only had a role similar to caspases in cell death but also in autophagy and this through different domains [55].

In caspase-independent programmed cell death, the increase in intracellular calcium increases mitochondrial calcium and causes further mitochondrial membrane depolarization, the generation of ROS, and the activation of endonucleases [56]. In the present study, we observed an increase in caspase-3/-7-like protease levels in cells following A3K2A3 exposure. Pretreatment with the caspase-3 inhibitor Ac-DEVD-CHO diminished cellular caspase-3/-7-like protease activity. Oligonucleosomal DNA fragmentation represents a late event of this programmed cell death pathway, leading to the passive release of DNA in the cytoplasm of apoptotic cells [57]. This also occurred in promastigotes that were treated with A3K2A3. Thus, DNA nicking in promastigotes strongly suggests that the anti-leishmanial effect is mediated by apoptosis-like cell death.

5. CONCLUSION

In conclusion, the present study found that the anti-leishmanial effect of A3K2A3 appears to be a consequence of the induction of apoptosis-like cell death that is caused by an increase in ROS levels inside cells. This increase is likely responsible for the collapse of mitochondrial membrane potential and depletion of ATP levels. A3K2A3 treatment also triggered apoptosis-like changes in *L. amazonensis* promastigotes, characterized by phosphatidylserine externalization, cell shrinkage, caspase activation, the induction of DNA fragmentation, and an increase in the number of cytoplasmic lipid droplets. This work provides some clues regarding the pathway by which *Leishmania* undergoes apoptosis and may pave the way for designing chemotherapeutic compounds against leishmaniasis.

ETHICAL APPROVAL: All of the animal procedures were performed in accordance with guidelines established by the Universidade Estadual de Maringá ethical committee (protocol no. 029/2014).

6. REFERENCES

1. Rajasekaran R, Chen Yi-Ping P (2015) Potential therapeutic targets and the role of technology in developing novel antileishmanial drugs. *Drug Discov Today* 20(8): 958–968. doi:10.1016/j.drudis.2015.04.006
2. Duszenko M, Figarella K, Macleod ET, Welburn SC (2006) Death of a trypanosome: a selfish altruism. *Trends Parasitol* 22(11): 536-542. doi:10.1016/j.pt.2006.08.010
3. Arambage SC, Grant KM, Pardo I, Ranford-Cartwright L, Hurd H. (2009) Malaria ookinetes exhibit multiple markers for apoptosis-like programmed cell death *in vitro*. *Parasit Vector* 2(1): 32. doi:10.1186/1756-3305-2-32
4. Kathuria M, Bhattacharjee A, Sashidhara KV, Singh SP, Mitra K (2014) Induction of mitochondrial dysfunction and oxidative stress in *Leishmania donovani* by orally active clerodane diterpene. *Antimicrob Agents Chemother* 58(10): 5916-5928. doi: 10.1128/AAC.02459-14
5. Din, ZU, Fill TP, de Assis FF, Lazzarin-Bidóia D, Kaplum V, Garcia FP, Nakamura CV, Oliveira KT, Rodrigues-Filho E (2014) Unsymmetrical 1, 5-diaryl-3-oxo-1, 4-pentadienyls and their evaluation as antiparasitic agents. *Bioorg Med Chem* 22(3): 1121-1127. doi:10.1016/j.bmc.2013.12.020
6. Shi M, Cai Q, Yao L, Mao Y, Ming Y, Ouyang G (2006). Antiproliferation and apoptosis induced by curcumin in human ovarian cancer cells. *Cell Biol Int* 30(3): 221-226. doi:10.1016/j.cellbi.2005.10.024
7. Aher RB, Wanare G, Kawathekar N, Kumar RR, Kaushik NK, Sahal D, Chauhan VS (2011) Dibenzylideneacetone analogues as novel *Plasmodium falciparum* inhibitors. *Bioorg Med Chem Lett* 21(10): 3034-3036. doi:10.1016/j.bmcl.2011.03.037
8. Prakobwong S, Gupta SC, Kim JH, Sung B, Pinlaor P, Hiraku Y, Wongkham S, Sripa B, Pinlaor S, Aggarwal BB (2011) Curcumin suppresses proliferation and induces apoptosis in human biliary cancer cells through modulation of multiple cell signaling pathways. *Carcinogenesis* 32(9): 1372-1380. doi: 10.1093/carcin/bgr032
9. Prakobwong S, Khoontawad J, Yongvanit P, Pairojkul C, Hiraku Y, Sithithaworn P, Pinlaor P, Aggarwa BB, Pinlaor S (2011) Curcumin decreases cholangiocarcinogenesis

in hamsters by suppressing inflammation-mediated molecular events related to multistep carcinogenesis. *Int J Cancer* 129(1): 88-100. doi: 10.1002/ijc.25656

10. Yu HJ, Shin JA, Nam JS, Kang BS, Cho SD (2013) Apoptotic effect of dibenzylideneacetone on oral cancer cells via modulation of specificity protein 1 and Bax. *Oral Dis* 19(8): 767-774. doi:10.1111/odi.12062

11. Prasad S, Yadav VR, Ravindran J, Aggarwal BB (2011) ROS and CHOP are critical for dibenzylideneacetone to sensitize tumor cells to TRAIL through induction of death receptors and downregulation of cell survival proteins. *Cancer Res* 71(2): 538-549. doi: 10.1158/0008-5472

12. Britta EA, Scariot DB, Falziroli H, Ueda-Nakamura T, Silva CC, Dias Filho BP, Borsali R, Nakamura CV (2014) Cell death and ultrastructural alterations in *Leishmania amazonensis* caused by new compound 4-Nitrobenzaldehyde thiosemicarbazone derived from S-limonene. *BMC Microbiol* 14(1): 236. doi: 10.1186/s12866-014-0236-0

13. Rodrigues JH da S, Ueda-Nakamura T, Corrêa AG, Sangi DP, Nakamura CV (2014) A Quinoxaline Derivative as a Potent Chemotherapeutic Agent, Alone or in Combination with Benznidazole, against *Trypanosoma cruzi*. *PLOS One*, 9(1):e85706. doi: 10.1371/journal.pone.0085706

14. Menna-Barreto RF, Goncalves RL, Costa EM, Silva RS, Pinto AV, Oliveira MF, de Castro SL (2009) The effects on *Trypanosoma cruzi* of novel synthetic naphthoquinones are mediated by mitochondrial dysfunction. *Free Radical Bio Med* 47(5): 644-653. doi:10.1016/j.freeradbiomed.2009.06.004

15. Shukla AK, Patra S, Dubey VK (2012) Iridoid glucosides from *Nyctanthes arbortristis* result in increased reactive oxygen species and cellular redox homeostasis imbalance in *Leishmania* parasite. *Eur J Med Chem* 54: 49-58. doi:10.1016/j.ejmech.2012.04.034

16. Takahashi M, Shibata M, Niki E (2001) Estimation of lipid peroxidation of live cells using a fluorescent probe, diphenyl-1-pyrenylphosphine. *Free Radical Bio Med* 31(2): 164-174. doi:10.1016/S0891-5849(01)00575-5

17. Lazarin-Bidóia D, Desoti VC, Ueda-Nakamura T, Dias Filho BP, Nakamura CV, Silva SO (2013) Further evidence of the trypanocidal action of eupomatenoid-5: confirmation of involvement of reactive oxygen species and mitochondria owing to a reduction in trypanothione reductase activity. *Free Radical Bio Med* 60: 17-28. doi:10.1016/j.freeradbiomed.2013.01.008
18. Britta EA, Silva AB, Ueda-Nakamura T, Dias-Filho BP, Silva CC, Sernaglia RL, Nakamura CV (2012) Benzaldehyde thiosemicarbazone derived from limonene complexed with copper induced mitochondrial dysfunction in *Leishmania amazonensis*. *PLOS One* 7(8): 1-12. doi: 10.1371/journal.pone.0041440
19. Stefanello TF, Panice MR, Ueda-Nakamura T, Sarragiotto MH, Auzély-Velty R, Nakamura CV (2014) N-Butyl-[1-(4-Methoxy)Phenyl-9H--Carboline]-3-Carboxamide Prevents Cytokinesis in *Leishmania amazonensis*. *Antimicrob Agents Chemother* 58 (12): 7112–7120. doi: 10.1128/AAC.03340-14
20. Jimenez V, Paredes R, Sosa MA, Galanti N (2008) Natural programmed cell death in *T. cruzi* epimastigotes maintained in axenic cultures. *J Cell Biochem* 105(3): 688-698. doi: 10.1002/jcb.21864
21. Kaur J, Singh BK, Tripathi RP, Singh P, Singh N (2009) *Leishmania donovani*: A glycosyl dihydropyridine analogue induces apoptosis like cell death via targeting pteridine reductase 1 in promastigotes. *Exp Parasitol* 123: 258–264. doi:10.1016/j.exppara.2009.07.009
22. Sen N, Das BB, Ganguly A, Mukherjee T, Tripathi G, Bandyopadhyay S, Rakshit S, Sen T, Majumder HK (2004). Camptothecin induced mitochondrial dysfunction leading to programmed cell death in unicellular hemoflagellate *Leishmania donovani*. *Cell Death Differ* 11(8): 924-936. doi:10.1038/sj.cdd.4401435
23. Arnoult D, Akarid K, Grodet A, Petit PX, Estaquier J, Ameisen JC (2002) On the evolution of programmed cell death: apoptosis of the unicellular eukaryote *Leishmania major* involves cysteine proteinase activation and mitochondrion permeabilization. *Cell Death Differ* 9:65–81. <http://dx.doi.org/10.1038/sj.cdd.4400951>.
24. Kulkarni MM, McMaster WR, Kamysz W, McGwire BS (2009) Antimicrobial Peptide-induced Apoptotic Death of *Leishmania* Results from Calcium-dependent,

Caspase-independent Mitochondrial Toxicity. *J Biol Chem* 284(23): 15496–15504. doi: 10.1074/jbc.M809079200

25. Goto H, Lindoso, JAL (2012) Cutaneous and mucocutaneous leishmaniasis. *Infect Dis Clin N Am* 26(2): 293-307. doi:10.1016/j.idc.2012.03.001

26. Bhandarkar SS, Bromberg J, Carrillo C, Selvakumar P, Sharma RK, Perry BN, Govindarajan B, Fried L, Sohn A, Reddy K, Arbiser JL (2008) Tris (dibenzylideneacetone) dipalladium, a N-myristoyltransferase-1 inhibitor, is effective against melanoma growth *In vitro* and *In vivo*. *Clin Cancer Res* 14(18): 5743-5748. doi: 10.1158/1078-0432.CCR-08-0405

27. Vendrametto MC, Santos AO, Nakamura CV, Dias Filho BP, Cortez DAG, Ueda-Nakamura T (2010) Evaluation of antileishmanial activity of eupomatenoid-5, a compound isolated from leaves of *Piper regnellii* var. *pallescens*. *Parasitol Int* 59(2): 154-158. doi:10.1016/j.parint.2009.12.009

28. Fernandes-Rodrigues JC., Souza WD (2008) Ultrastructural alterations in organelles of parasitic protozoa induced by different classes of metabolic inhibitors. *Curr Pharm Des* 14(9): 925-938. doi: <http://dx.doi.org/10.2174/138161208784041033>

29. Kathuria M, Bhattacharjee A, Sashidhara KV, Singh SP, Mitra K (2014) Induction of Mitochondrial Dysfunction and Oxidative Stress in *Leishmania donovani* by Orally Active Clerodane Diterpene . *Antimicrob Agents Chemother* 58 (10): 5916–5928. doi: 10.1128/AAC.02459-14

30. Kafetzis DA, Velissariou IM, Stabouli S, Mavrikou M, Delis D, Liapi G (2005) Treatment of paediatric visceral leishmaniasis: amphotericin B or pentavalent antimony compounds? *Int J Antimicrob Agents* 25:26–30. doi:10.1016/j.ijantimicag.2004.09.011

31. Tiuman TS, Ueda-Nakamura T, Cortez DAG, Dias-Filho BP, Morgado-Díaz JA, Souza W, Nakamura CV (2005) Antileishmanial activity of parthenolide, a sesquiterpene lactone isolated from *Tanacetum parthenium*. *Antimicrob Agents Chemother* 49:176–82. doi: 10.1128/AAC.49.11.176-182.2005

32. Ueda-Nakamura T, Mendonça-Filho RR, Morgado-Díaz JA, Maza PK, Dias-Filho BP, Cortez DAG, et al (2006) Antileishmanial activity of Eugenol-rich essential oil

from *Ocimum gratissimum*. *Parasitol Int* 55(2):99–105.
doi:10.1016/j.parint.2005.10.006

33. Inácio JDF, Canto-Cavalheiro MM, Menna-Barreto RFS, Almeida-Amaral EE (2012) Mitochondrial damage contribute to epigallocatechin-3-gallate induced death in *Leishmania amazonensis*. *Exp Parasitol* 132(2):151–155.
doi:10.1016/j.exppara.2012.06.008

34. Medina JM, Rodrigues JCF, De Souza W, Atella GC, Barrabim H (2012) Tomatidine promotes the inhibition of 24-alkylated sterol biosynthesis and mitochondrial dysfunction in *Leishmania amazonensis* promastigotes. *Cambridge Univ Press* 139(10):1253–1265. doi: <http://dx.doi.org/10.1017/S0031182012000522>

35. Bringaud F, Rivière L, Coustou V (2006) Energy metabolism of trypanosomatids: Adaptation to available carbon sources. *Mol Biochem Parasit* 149:1–9.
doi:10.1016/j.molbiopara.2006.03.017

36. Sen N, Das BB, Ganguly A, Mukherjee T, Bandyopadhyay S, Majumder HK (2004) Camptothecin-induced imbalance in intracellular cation homeostasis regulates programmed cell death in unicellular hemoflagellate *Leishmania donovani*. *J Biol Chem* 279(50): 52366-52375. doi: 10.1074/jbc.M406705200

37. Mukherjee SB, Das M, Sudhandiran G, Shaha C (2002) Increase in Cytosolic Ca²⁺ Levels through the Activation of Non-selective Cation Channels Induced by Oxidative Stress Causes Mitochondrial Depolarization Leading to Apoptosis-like Death in *Leishmania donovani* Promastigotes. *J Biol Chem* 277(27): 24717-24727. doi: 10.1074/jbc.M201961200

38. Chowdhury S, Mukherjee T, Chowdhury SR, Sengupta S, Mukhopadhyay S, Jaisankar P, Majumder HK (2014) Disuccinyl Betulin Triggers Metacaspase-Dependent Endonuclease G-Mediated Cell Death in Unicellular Protozoan Parasite *Leishmania donovani*. *Antimicrob Agents Chemother* 58(4), 2186-2201. doi: 10.1128/AAC.02193-13

39. Kowaltowski AJ, de Souza-Pinto NC, Castilho RF, Vercesi AE (2009) Mitochondria and reactive oxygen species. *Free Radical Bio Med* 47(4): 333-343.
doi:10.1016/j.freeradbiomed.2009.05.004

40. Smirlis D, Duszenko M, Ruiz AJ, Scoulica E, Bastien P, Fasel N, Soteriadou K (2010) Targeting essential pathways in trypanosomatids gives insights into protozoan mechanisms of cell death. *Parasite Vector* 3:107. doi:10.1186/1756-3305-3-107
41. Fonseca-Silva F, Inacio JD, Canto-Cavalheiro MM, Almeida-Amaral EE (2011) Reactive oxygen species production and mitochondrial dysfunction contribute to quercetin induced death in *Leishmania amazonensis*. *PLOS One* 6(2): e14666. doi: 10.1371/journal.pone.0014666
42. Islamuddin M, Chouhan G, Tyagi M, Abdin MZ, Sahal D, Afrin F (2014) Leishmanicidal activities of *Artemisia annua* leaf essential oil against Visceral Leishmaniasis. *Front Microbiol* 5:626. doi: 10.3389/fmicb.2014.00626
43. Mehta A, Shaha C (2006) Mechanism of metalloid-induced death in *Leishmania* spp.: Role of iron, reactive oxygen species. Ca²⁺ and glutathione. *Free Radical Bio Med* 40:1857–1868. doi:10.1016/j.freeradbiomed.2006.01.024
44. Mandal G, Wyllie S, Singh N, Sundar S, Fairlamb AH, Chatterjee M (2007) Increased levels of thiols protect antimony unresponsive *Leishmania donovani* field isolates against reactive oxygen species generated by trivalent antimony. *Parasitology* 134(12): 1679-1687. doi: <http://dx.doi.org/10.1017/S0031182007003150>
45. Sarkar A, Mandal G, Singh N, Sundar S, Chatterjee M (2009) Flow cytometric determination of intracellular non-protein thiols in *Leishmania* promastigotes using 5-chloromethyl fluorescein diacetate. *Exp Parasitol* 122(4): 299-305. doi:10.1016/j.exppara.2009.04.012
46. Koonin EV, Aravind L (2002) Origin and evolution of eukaryotic apoptosis: the bacterial connection. *Cell Death Differ* 9(4): 394-404. doi: 10.1038/sj/cdd/4400991
47. Mehta A, Shaha C (2004) Apoptotic Death in *Leishmania donovani* promastigotes in Response to Respiratory Chain Inhibition complex II inhibition results in increased pentamidine cytotoxicity. *J Biol Chem* 279(12): 11798-11813. doi: 10.1074/jbc.M309341200
48. Dutta A, Ghoshal A, Mandal D, Mondal NB, Banerjee S, Sahu NP, Mandal C (2007) Racemoside A, an anti-leishmanial, water-soluble, natural steroidal saponin,

induces programmed cell death in *Leishmania donovani*. J Med Microbiol 56(9): 1196-1204. doi: 10.1099/jmm.0.47114-0

49. Kroemer G, Galluzzi L, Vandenabeele P et al (2009) Classification of cell death: recommendations of the Nomenclature Committee on Cell Death 2009,” Cell Death Differ 16 (1): 3–11. doi:10.1038/cdd.2008.150

50. Igney FH, Krammer PH (2002) Death and anti-death: tumour resistance to apoptosis. Nat Rev Cancer 2(4): 277-288. doi:10.1038/nrc776

51. Ryter SW, Kim HP, Hoetzel A, Park JW, Nakahira K, Wang X, Choi AM (2007) Mechanisms of cell death in oxidative stress. Antioxid Redox Sign 9(1): 49-89. doi:10.1089/ars.2007.9.49

52. Facompre M, Goossens JF, Bailly C (2001) Apoptotic response of HL-60 human leukemia cells to the antitumor drug NB-506, a glycosylated indolocarbazole inhibitor of topoisomerase 1. Biochem Pharmacol 61(3): 299-310. doi:10.1016/S0006-2952(00)00553-0

53. Kosec G, Alvarez VE, Agüero F, Sánchez D, Dolinar M, Turk B, Turk V, Cazzulo JJ (2006) Metacaspases of *Trypanosoma cruzi*: possible candidates for programmed cell death mediators. Mol Biochem Parasitol 145:18–28. doi: 10.1016/j.molbiopara.2005.09.001

54. Lee N, Gannavaram S, Selvapandiyan A, Debrabant A (2007) Characterization of metacaspases with trypsin-like activity and their putative role in programmed cell death in the protozoan parasite *Leishmania*. Eukaryot Cell 6:1745–1757. doi: 10.1128/EC.00123-07

55. Casanova M, Gonzalez IJ, Sprissler C, Zalila H, Dacher M, Basmaciyan L, Späth G F, Azas N, Fasel N (2015) Implication of different domains of the *Leishmania major* metacaspase in cell death and autophagy. Cell Death Dis 6(10): e1933. doi: 10.1038/cddis.2015.288

56. Martinvalet D, Zhu P, Lieberman J (2005) Granzyme A induces caspase-independent mitochondrial damage, a required first step for apoptosis. Immunity 22(3): 355-370. doi:10.1016/j.immuni.2005.02.004

57. Zangger H, Mottram JC, Fasel N (2002) Cell death in *Leishmania* induced by stress and differentiation: programmed cell death or necrosis? *Cell Death Differ* 9(10): 1126-1139. doi:10.1038/sj.cdd.4401071

7. Figures

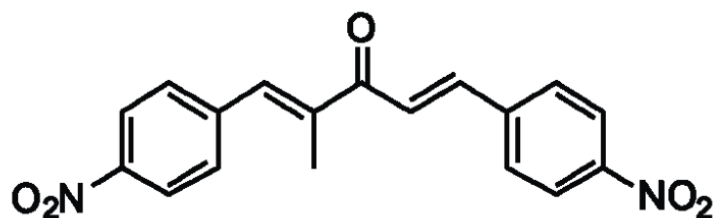


Fig. 1 Chemical structure of (1E,4E)-2-methyl-1,5-bis(4-nitrophenyl)penta-1,4-dien-3-one (A3K2A3).

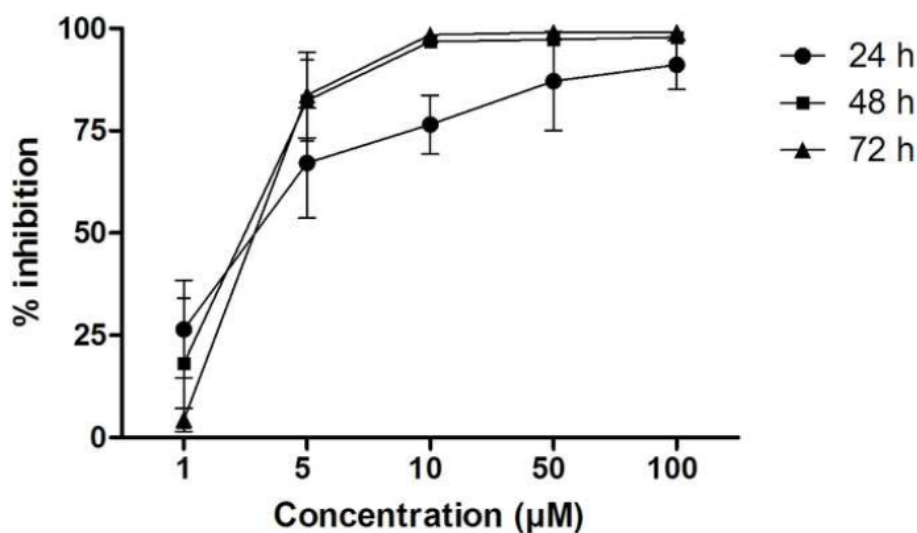


Fig. 2 Effect of A3K2A3 on promastigote forms of *Leishmania amazonensis*. Promastigotes were treated with 1, 5, 10, 50, and 100 µM A3K2A3 and counted daily in a Neubauer chamber until 72 h of incubation. The graph of concentration vs. percentage growth inhibition was plotted each day, and inhibitory concentrations were determined. Symbols represent the mean \pm standard deviation of at least two independent experiments, which were performed in duplicate.

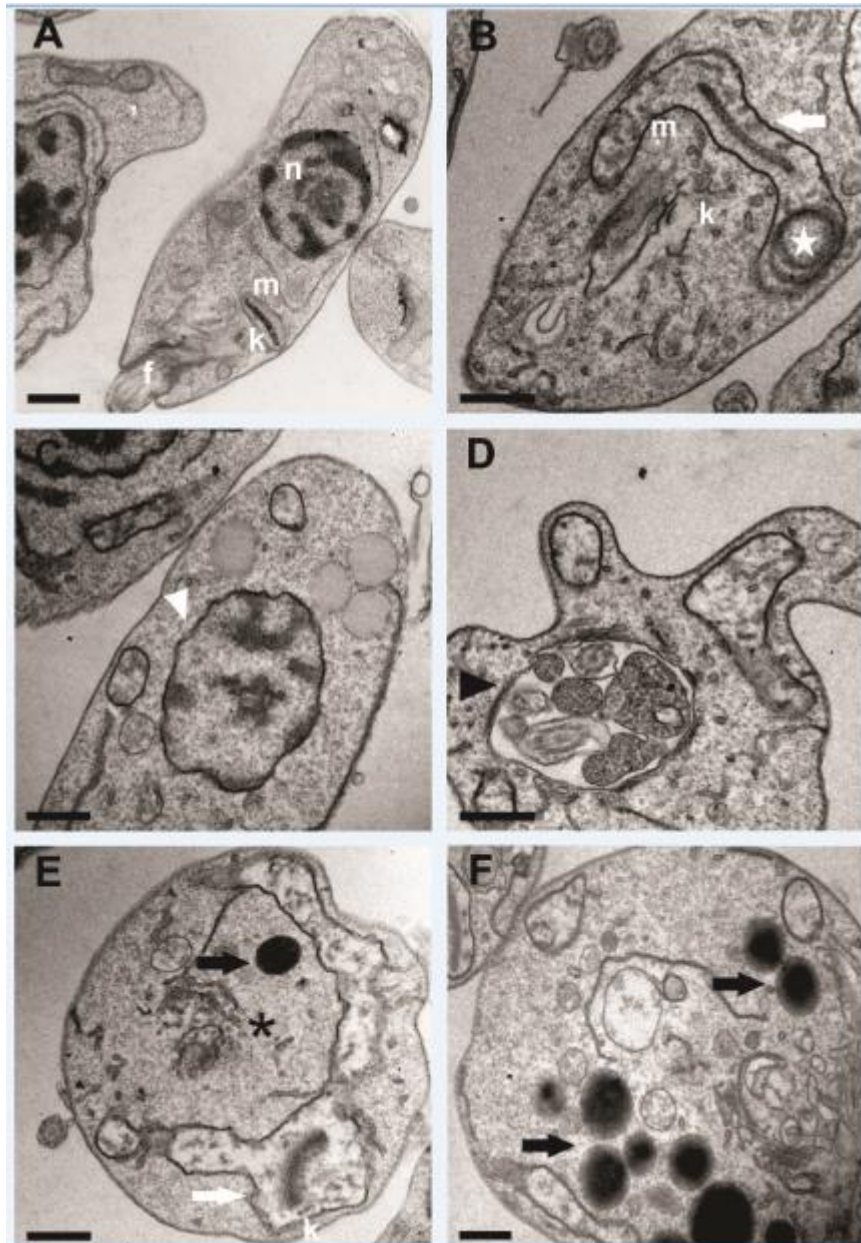


Fig. 3 Ultrathin sections of *Leishmania amazonensis* promastigotes. (A) Without treatment, presenting a normal ultrastructure and promastigotes treated with A3K2A3 at concentrations that corresponded to the IC₅₀ (B-D) and IC₉₀ (E-F). White arrows indicate swollen mitochondria. Black arrows represent lipid-storage bodies. Black arrowheads indicate the presence of vesicles inside the flagellar pocket. White arrowheads indicate DNA disorganization in nuclei. The star indicates the presence of concentric membranous structures. The asterisk indicates Golgi complex disorganization. n, nucleus; m, mitochondrion; k, kinetoplast; f, flagellum; fp, flagellar pocket. Scale bar = 0.5 μ m.

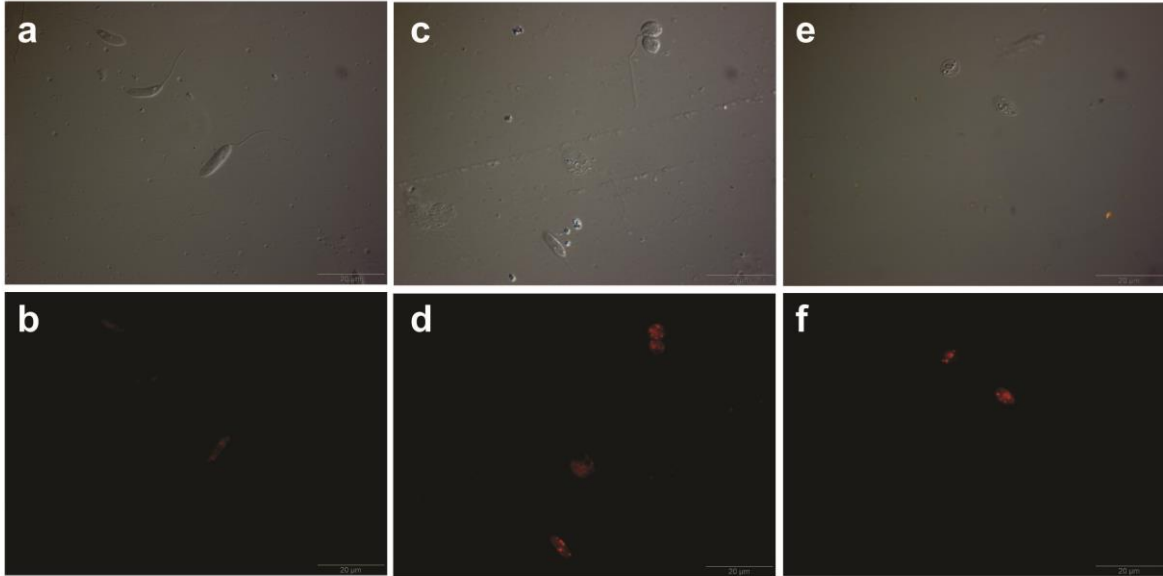
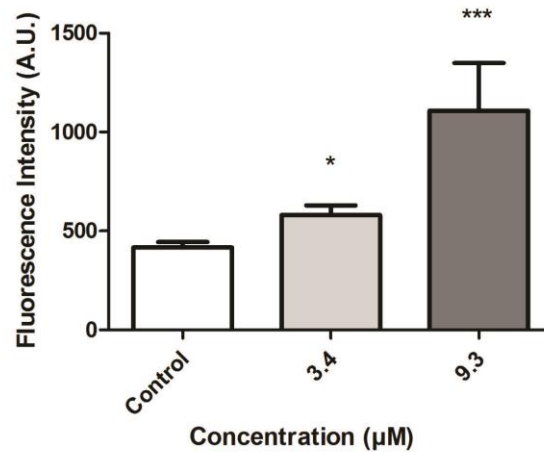
A**B**

Fig. 4 (A) Differential interference contrast microscopy (DIC) and fluorescence microscopy with Nile Red staining of *Leishmania amazonensis* promastigotes without treatment (a,b) and treated with A3K2A3 at concentrations of 3.4 μM (c, d) and 9.3 μM (e, f) for 24 h. In treated promastigotes, images suggest accumulation of lipid-storage bodies in the cytoplasm (B, D, F). Scale bar = 10 μm. (B) Accumulation of lipid-storage bodies in promastigote forms of *L. amazonensis* treated with A3K2A3 at the IC₅₀ and IC₉₀ for 24 h using the fluorescent probe Nile Red. The data are expressed as the mean fluorescence (in arbitrary units) ± SD of at least three independent experiments. * $p \leq 0.05$, significant difference compared with the negative control group (i.e., untreated parasites).

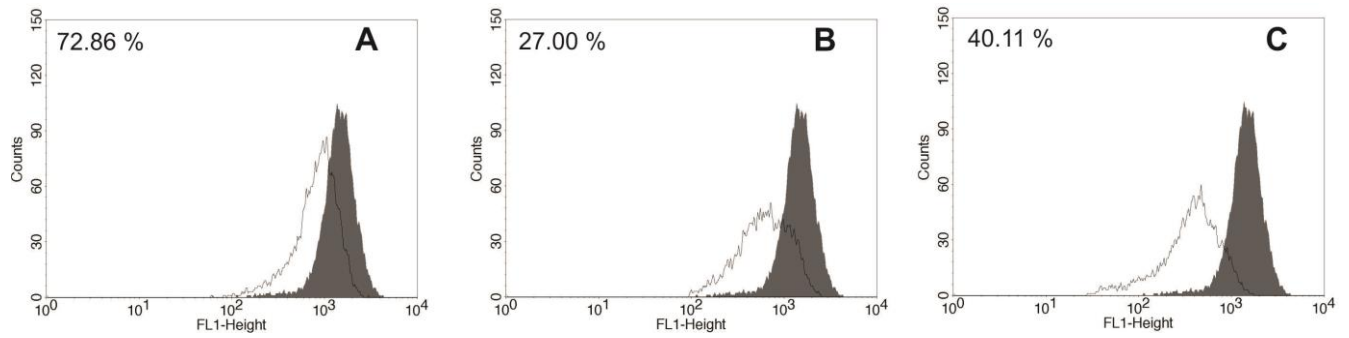


Fig. 5 Mitochondrial membrane potential assay in promastigote forms of *L. amazonensis*. (A) Positive control (CCCP). (B) Promastigotes treated with A3K2A3 at concentrations of 3.4 μ M and 9.3 μ M (C) for 24 h and stained with Rh123, which accumulates in mitochondria. The gray area corresponds to the negative control group (i.e., untreated parasites). Typical histograms of at least three independent experiments are shown.

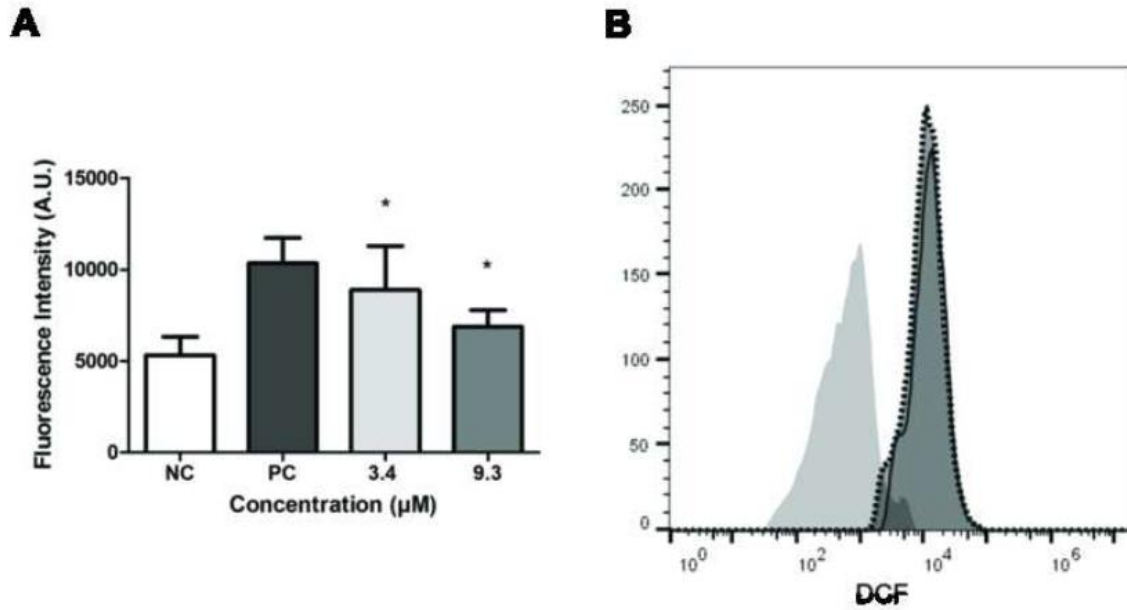


Fig. 6 (A) Total ROS production in promastigote forms of *L. amazonensis* treated with A3K2A3 at concentrations of 3.4 and 9.3 μM for 24 h using the fluorescent probe H₂DCFDA. Data are expressed as the mean fluorescence (in arbitrary units) \pm SD of at least three independent experiments. Hydrogen peroxide (20 mM) was used as a positive control (PC). * $p \leq 0.05$, significant difference compared with the negative control group (i.e., untreated parasites). **(B)** Flow Cytometry histograms showing the total ROS production in promastigote forms of *L. amazonensis* treated with A3K2A3 at concentrations of 3.4 and 9.3 μM for 24 h using the fluorescent probe H₂DCFDA. Control untreated cells: light gray filled area; 3.4 μM treated cells: dashed-line surrounded gray filled area; 9.3 μM solid-line surrounded gray filled area.

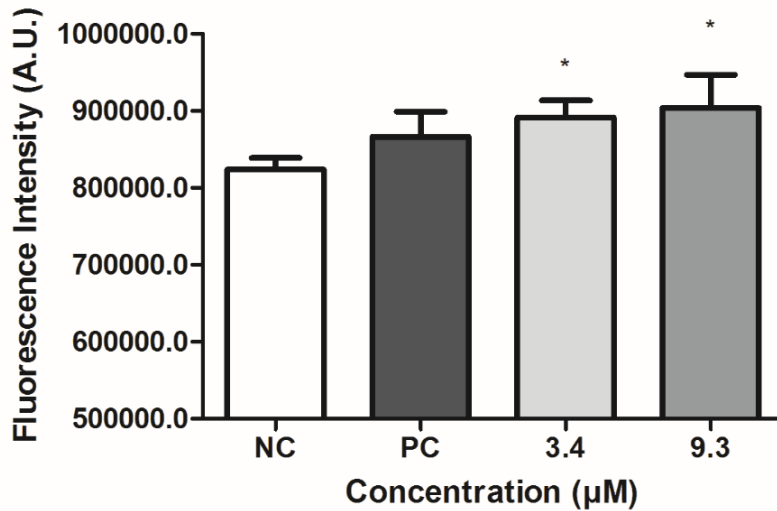


Fig. 7 Formation of hydroperoxides in promastigotes treated with the IC₅₀ and IC₉₀ of A3K2A3. DPPP-labeled cells were evaluated by measuring the fluorescence intensity after 24 h of treatment. Hydrogen peroxide (200 µM) was used as a positive control (PC). The data are expressed as the mean ± SD of at least three independent experiments in triplicate. * $p \leq 0.05$, significant difference compared with the negative control group (i.e., untreated parasites).

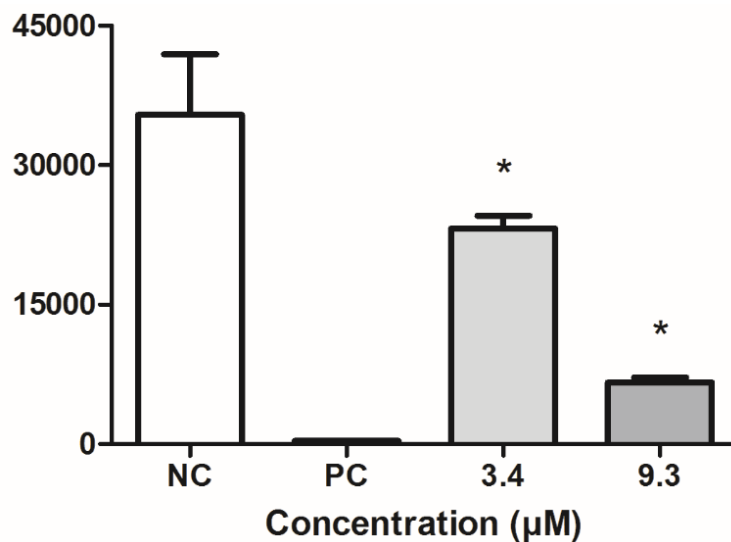


Fig. 8 Determination of the level of intracellular ATP using CellTiter-Glo reagent after treatment with A3K2A3 at concentrations of 3.4 and 9.3 µM for 24 h. CCCP (100 µM) was used as a positive control. The data are expressed as the mean ± SD of three independent experiments. * $p \leq 0.05$, significant difference compared with the negative control group (i.e., untreated parasites). CCCP (100 µM) was used as a positive control.

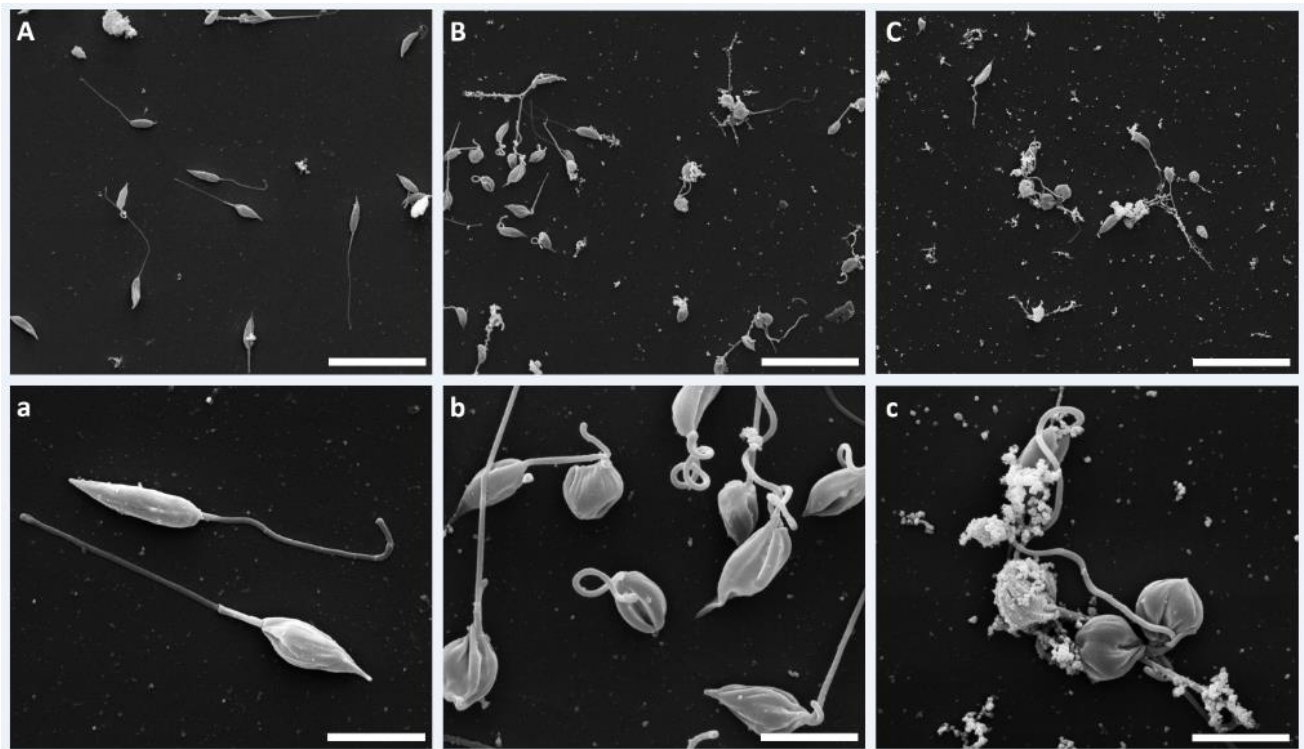


Fig. 9 Scanning electron microscopy images of promastigote forms of *L. amazonensis* incubated in the absence (A) or presence of A3K2A3 at concentrations of 3.4 μM (B) and 9.3 μM (C) for 72 h. Scale bar = 20 μm (A-C) and 5 μm (a-c).

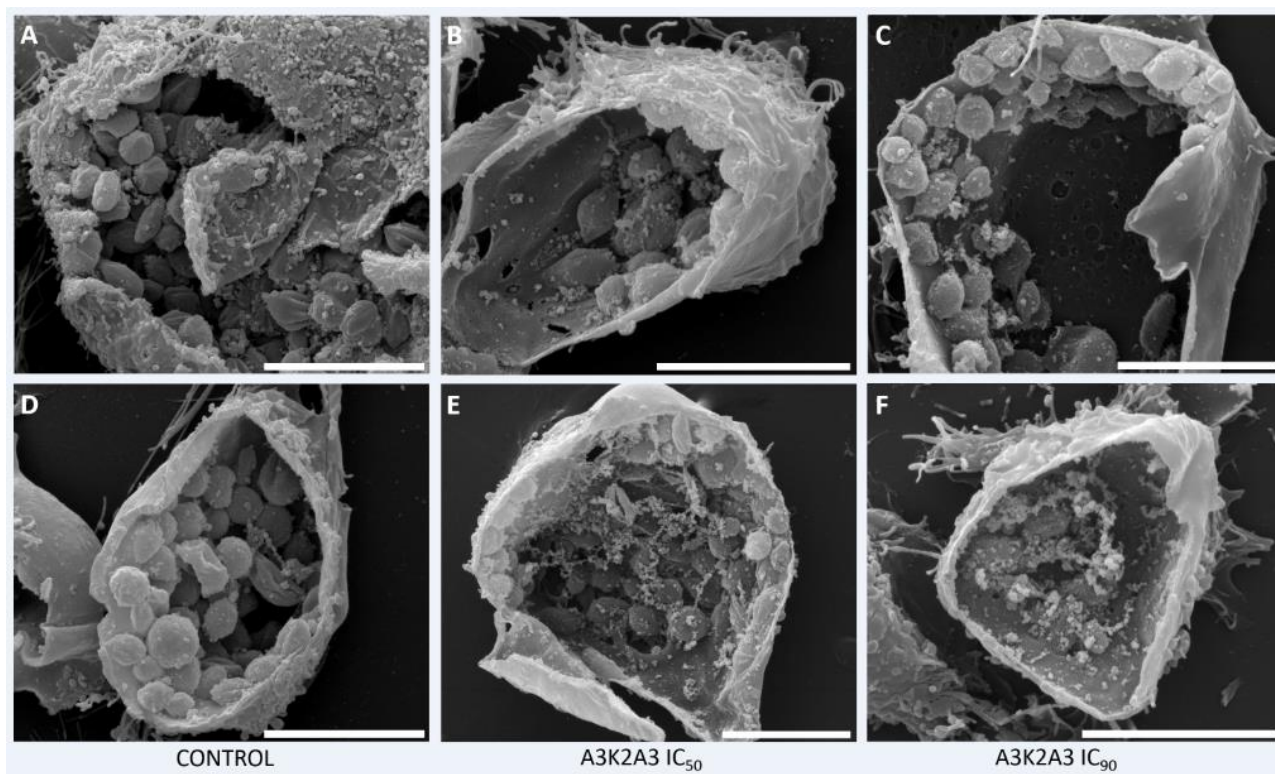


Fig. 10 Scanning electron microscopy images of intracellular amastigotes forms of *L. amazonensis* incubated in the absence (A and D) or presence of A3K2A3 at concentrations of 3.4 μM (B and E) and 9.3 μM (C and F) for 72 h. Scale bar = 10 μm (A-F).

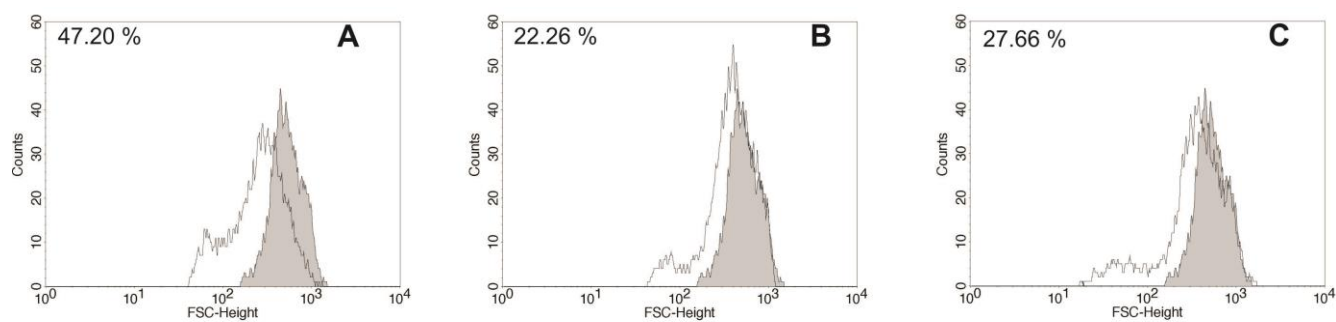


Fig. 11 Cell volume in promastigote forms of *L. amazonensis* treated with A3K2A3 at concentrations of 3.4 μM (B) and 9.3 μM (C) for 24 h. Actinomycin D (20.0 mM) was used as a positive control (A). FSC-H was considered a function of cell size. The gray area corresponds to the negative control group (i.e., untreated parasites). Typical histograms of at least three independent experiments are shown.

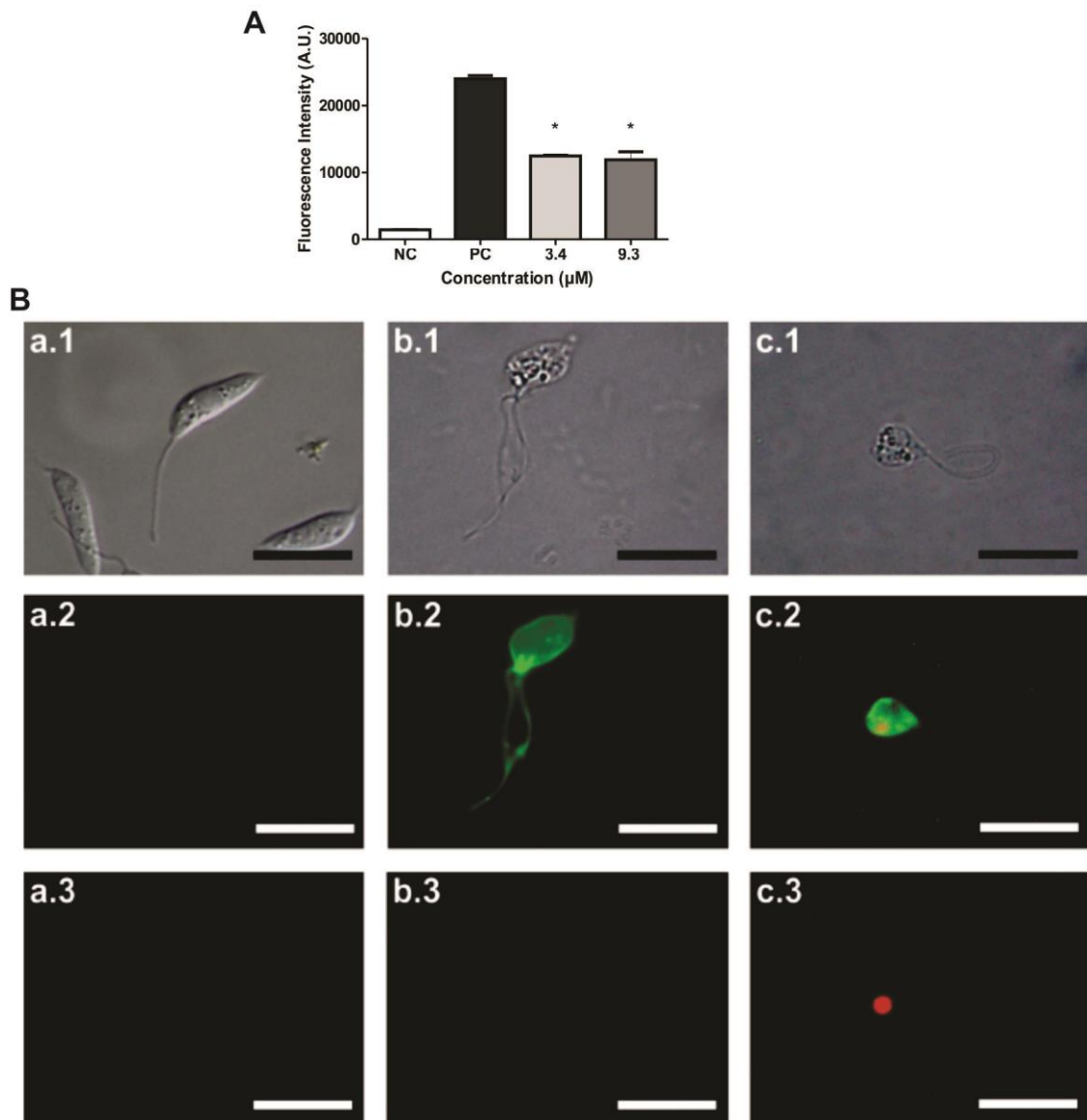


Fig. 12 (A) Phosphatidylserine exposure in promastigote forms of *L. amazonensis* treated with A3K2A3 at concentrations of 3.4 and 9.3 μM for 24 h using annexin V-FITC. Negative control (NC; i.e., untreated parasites). Antimycin A (125.0 μM) was used as a positive control (PC). A typical graph of at least three independent experiments is shown. (B) Differential interference contrast microscopy (DIC) in a.1, b.1, c.1 and fluorescence microscopy of *Leishmania amazonensis* promastigotes after Annexin-V-FITC (a.2; b.2 and c.2) and Propidium Iodide staining (a.3; b.3 and c.3). Control parasites were kept untreated (A) and the treated were incubated with A3K2A3 at concentrations of 3.4 μM (B) and 9.3 μM (C) for 24 h. Bars: 10 μm

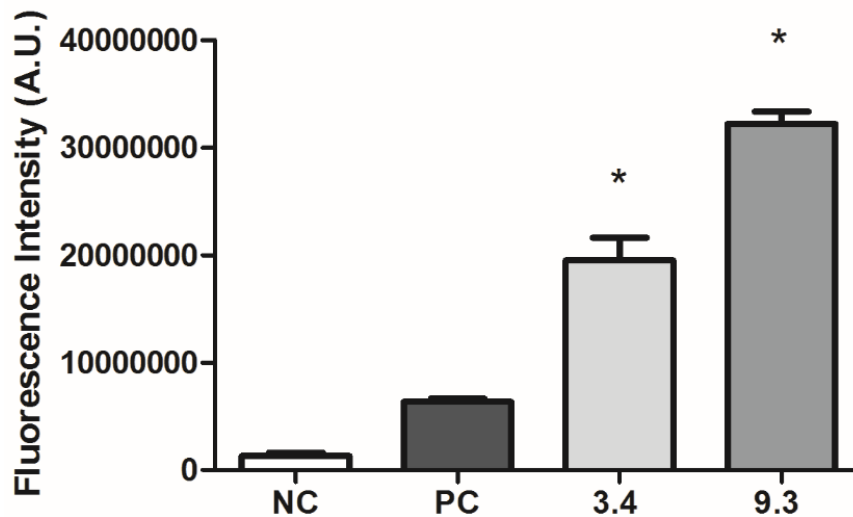


Fig. 13 Activity of caspase-3/7-like proteases in promastigotes that were treated with A3K2A at concentrations of 3.4 and 9.3 μM for 24 h using the fluorescent EnzCheck Caspase-3 Assay kit. Camptothecin (20 μM) was used as a positive control (PC). The specificity of activity was tested by preincubating the cells with a caspase-3-specific inhibitor prior to the analysis of caspase-3/7 activity. The data are expressed as the mean \pm SD from three independent experiments. * $p \leq 0.05$, significant difference compared with the negative control (NC) group (i.e., untreated parasites).

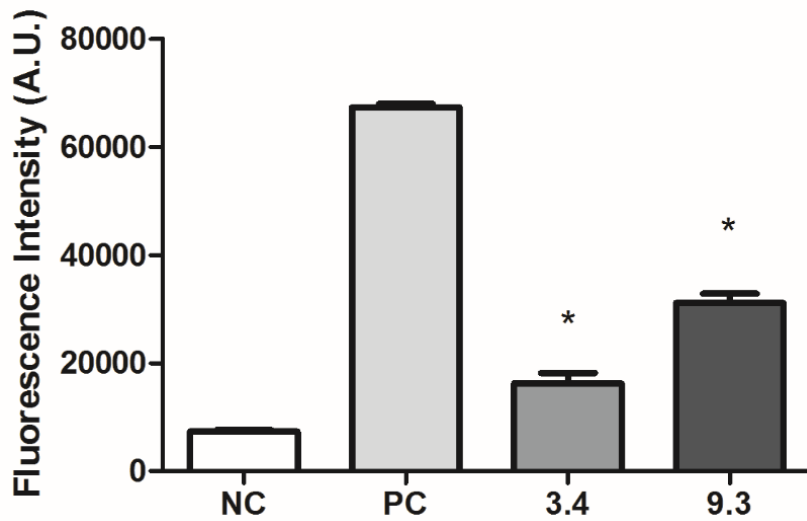


Fig. 14 DNA fragmentation in promastigotes treated with A3K2A3 at the IC₅₀ and IC₉₀ for 24 h using the TUNEL assay. Camptothecin (20 μ M) was used as a positive control (PC). The data are expressed as the mean \pm SD from three independent experiments. * $p \leq 0.05$, significant difference compared with the negative control (NC) group (i.e., untreated parasites).

Artigo 2

Tuning the stability of self-assembled nanogels based on hyaluronic acid using ketone-hydrazide cross-linking

*Francielle P. Garcia^{a,b,c}, Mychelle Vianna^c, Talitha F. Stefanello^{a,b,c}, Marlène Rippe^{a,b}, Benoit Louage^d, Simon Van Herck,^d Lucie Sancey^e, Jean-Luc Coll^e, Bruno G. De Geest^d, Celso V. Nakamura^c, Rachel Auzély-Velty^{*a,b}*

^aGrenoble Alpes University and Centre de Recherches sur les Macromolécules Végétales, 601, rue de la Chimie, BP53, 38041 Grenoble Cedex 9, France

^bCNRS and Centre de Recherches sur les Macromolécules Végétales, 601, rue de la Chimie, BP53, 38041 Grenoble Cedex 9, France

^cLaboratory of technological innovation in the development of pharmaceuticals and cosmetics, State, University of Maringa, Maringa, Brazil

^dDepartment of Pharmaceutics, Ghent University, 9000 Ghent, Belgium

^eGrenoble Alpes University and INSERM U823, Institut Albert Bonniot, La Tronche, Grenoble Cedex 9, France

ABSTRACT

The development of biopolymer-based nanogels has gained particular interest in order to achieve successful delivery of therapeutics for the treatment of various diseases, such as cancer, infection and diabetes. Herein, we report a new and simple methodology for the covalent stabilization of self-assembled gel nanoparticles based on hyaluronic acid (HA) modified with a thermoresponsive ketone-functional copolymer. This relies on the selective formation of crosslinks within the hydrophobic domains of the globular copolymer chains by hydrazone bond formation with a bifunctional hydrazide crosslinker. This approach allows to tune the crosslinking density by varying the dihydrazide crosslinker:ketone molar ratio. The main advantage of these new nanogels, over non-crosslinked nanogels, is that they have significantly improved stability, while maintaining the intrinsic biological properties of HA as a potential targeting agent to cancer cells. Interestingly, this crosslinking strategy did not affect the encapsulation efficiency of the nanogels. Their potential to deliver hydrophobic agents into cancer cells overexpressing the CD44 receptor of HA was also demonstrated from *in vitro* cellular uptake studies and cytotoxicity assays. Following intravenous injection of Cy5.5-labeled nanogels into tumor-bearing mice, full body fluorescence imaging indicated that the crosslinked nanogels could efficiently accumulate in tumor tissue. Because of their unique structures and properties, these novel core-crosslinked nanogels could potentially provide a new nanomedicine platform for the treatment of various diseases, especially cancer through passive and active tumor targeting.

KEYWORDS: hyaluronic acid; self-assembly; thermoresponsive nanogels; crosslinking; drug delivery; tumor targeting

1. Introduction

Self-assembled gel nanoparticles (also called nanogels) made of hydrophobically modified biopolymers have attracted growing interest for drug delivery to tumors as these systems combine the advantages of hydrogels with nanoscale formulations.¹⁻⁴ Their size can be easily varied from one hundred to several hundred nanometers, their interior network comprising hydrophobic domains can be used to incorporate poorly water-soluble drugs and their hydrophilic shell can be exploited to control their biological fate and targeting ability. However, one practical challenge with such carrier systems is their tendency to disassemble in the bloodstream because of the large dilution volume and/or interactions with biomolecules.⁵ These negative events reduce the efficiency of tumor-targeted drug delivery via the enhanced permeability and retention (EPR) effect⁶.

To stabilize nanocarriers, strategies of shell or core crosslinking have been employed.⁷⁻¹¹ Among these methods, crosslinking the hydrophobic domains in the nanogel core rather than the hydrophilic shell has the advantage of preserving the intrinsic properties of the biopolymer forming the hydrophilic shell. In particular, in the case of hyaluronic acid, a natural polysaccharide that has been widely explored for anticancer drug delivery,¹²⁻¹⁴ care must be taken regarding the conditions for its chemical crosslinking if the aim is to additionally exploit its potential to target cancer cells. Indeed, HA-cell receptor interaction is critically dependent on the molar mass and conformational freedom of HA.^{15, 16} Thus, HA6, which is three HA disaccharide units, is the minimum size of HA chain required to occupy the binding site of CD44 receptors that are overexpressed by several cancer cells, while HA10 or greater is the optimal length.¹⁷ Therefore, too high a degree of modification or crosslinking of HA could potentially affect its biological behavior.¹⁸⁻²¹

In this study, we aimed to establish a simple and reliable method for the synthesis of core-crosslinked nanogels based on hyaluronic acid, for improved nanogel stability in view of *in vivo* tumor-targeted drug delivery. Key to our strategy is the chemical modification of HA by a temperature-responsive keto-functional polymer which can be efficiently crosslinked by bifunctional hydrazides in aqueous medium (Scheme 1). Keto-functionalized polymers have been demonstrated to be useful reactive scaffolds for the design of complex macromolecular architectures and the conjugation

of fragile biomolecules since they can be modified easily and in high yield.²²⁻²⁵ Herein, the keto-polymer plays a dual role : i) in inducing self-assembly of modified HA into nanogels due to the formation of hydrophobic domains in response to temperature increase , and ii) in stabilizing the nanogel structure through crosslinking by hydrazone bond formation between ketones and hydrazides. We further show that the anticancer drug paclitaxel (PTX) can be entrapped into the nanogels and delivered intracellularly in cancer cells. In addition, we investigated the *in vivo* biodistribution and demonstrate tumor targeting potential of Cy5.5-labeled crosslinked nanogels.

2. Materials and Methods

Materials. Hyaluronic acid ($M_w = 40$ kg/mol) was purchased from Lifecore (USA). Diacetone acrylamide (DAAM), *N,N*-dimethylacrylamide (DMA), 2,2-azobis(2-methylpropionitrile) (AIBN), phosphate buffer saline (PBS, pH 7.4), Tris-(2-carboxyethyl) phosphine hydrochloride (TCEP), mercaptopropionic acid (MPA), 3-(4,5-dimethylthiazol-2-yl)-2,5-diphenyltetrazolium bromide (MTT) and 4-(4,6-dimethoxy-1,3,5-triazin-2-yl)-4-methylmorpholinium chloride (DMTMM) were purchased from Sigma-Aldrich-Fluka (France). Aminoethylmaleimide hydrochloride was purchased from Aokchem. *N*-hydroxysulfosuccinimide sodium salt (sulfo-NHS) was obtained from Chemrio. *N*-(3-dimethylaminopropyl)-*N'*-ethylcarbodiimide hydrochloride (EDC) and Paclitaxel (PTX) were purchased from Acros Organics. Dulbecco's Modified Eagle Medium (DMEM), L-glutamine, sodium pyruvate, fetal bovine serum (FBS), penicillin and streptomycin were provided by Gibco. Cyanine 5-amine (Cy5-amine) and Cyanine 5.5-amine (Cy5.5-amine) were purchased from Lumiprobe. All chemicals were used without any further purification. The positively charged resin, diethylaminoethyl cellulose (DEAE) was purchased from GE Healthcare Life Science. 2-(Butylthiocarbonothioylthio)propanoic acid (PABTC) was synthesized as previously reported²⁶. The dye di-strylbenzene derivative (DSB) was kindly provided by Olivier Stephan (Grenoble Alpes University, Grenoble, France). The water used in all experiments was purified by a Elga Purelab purification system, with a resistivity of 18.2 M Ω cm.

Analytical Techniques. ^1H NMR spectra were recorded at 25 °C using a Bruker AVANCE III HD spectrometer operating at 400 MHz. Deuterium oxide (D_2O) and dimethylsulfoxide- d_6 ($\text{DMSO-}d_6$) were obtained from SDS (Vitry, France). All spectra were recorded by applying a 45° tip angle for the excitation pulse, and a 10 s recycle delay. Chemical shifts (δ in ppm) are given relative to external tetramethylsilane (TMS = 0 ppm) and calibration was performed using the signal of the residual protons of the solvent as a secondary reference. The number-average molar mass (M_n), the weight-average molar mass (M_w) and the dispersity (D) of poly(DAAM-co-DMA) were determined by size exclusion chromatography (SEC) in tetrahydrofuran at 40°C with a flow rate of 1 mL/min and were derived from the refractive index (RI) signal by a calibration curve based on polystyrene (PS) standards. The cloud point temperature (T_{cp}) of poly(DAAM-co-DMA) was determined by UV/vis turbidity measurements performed on a Varian Cary 50 Scan. The samples were prepared at room temperature in deionized water (1 and 3 g/L), after which the sample was placed in the instrument. The light transmittance was measured during at least two controlled cooling/heating cycles from 15 °C to 35 °C using a 2 °C interval. T_{CP} was considered to be the temperature at which the light transmittance was 50 % of that obtained for the same sample at 15 °C. The critical aggregation temperature (CAT) of HA-m-poly(DAAM-co-DMA) in aqueous solution was assessed by static light scattering (SLS) using a ALV 5000 device (ALV-Langen, Germany) equipped with a red helium-neon laser at a wavelength of 632.8 nm. A solution of HA-m-poly(DAAM-co-DMA) in PBS at a concentration of 0.5 mg/mL was filtered through a 1.2 μm polycarbonate filter and heated from 10 to 50 °C using a 5 °C interval. The light scattering intensity (LSI) was measured at 90° angle for 60 s. The CAT, defined as the temperature at the inflection point of the plotted curve, was found to be 32 °C. The size and size distribution of nanogels were measured by dynamic light scattering (DLS) using a Zetasizer NanoZS Malvern Instruments apparatus operating with a HeNe laser at 173°. The hydrodynamic diameters were calculated from diffusion coefficients using the Stokes-Einstein equation. All correlogram analyses were performed with software supplied by the manufacturer. All the measurements were performed in PBS (pH 7.4, $[\text{NaCl}] = 0.15 \text{ M}$).

Synthesis of copolymer poly(DAAM-co-DMA). DMA (1.055 mL, 6.6 mmol) and DAAM (2.267 g, 13.4 mmol), the RAFT agent PABTC (47.7 mg, 0.2 mmol) and

AIBN (6.57 mg, 0.04 mmol) in 8.5 mL anhydrous dioxane were placed into a Schlenk tube under nitrogen. After 5 freeze-pump-thaw deoxygenation of the solution, the resulting solution was immersed in a thermostated oil bath at 75 °C and left to react for 3 h. The reaction was stopped by quenching. The resulting polymer was precipitated in cold hexane followed by centrifugation. The precipitate was dissolved in acetone and the copolymer was precipitated again in hexane. This step was repeated 3 times to give 3.35 g of pure copolymer.

Synthesis of HA-m-poly(DMA-co-DAAM). Prior to the coupling reaction with HA-maleimide, the poly(DAAM-co-DMA) copolymer was subjected to aminolysis using *n*-butylamine, to convert the RAFT end-group to a thiol. Briefly, the copolymer (0.370 g, 0.225 mmol) was solubilized in tetrahydrofuran (10 mL) and *n*-butylamine (4 mL, 0.04 mol) was added. After 5 min under stirring, the reaction mixture was concentrated under reduced pressure, resulting in a waxy liquid that was solubilized in THF. The copolymer was recovered by precipitation in cyclohexane and dried under vacuum at 45 °C to obtain a white powder. Next, the thiol-capped copolymer (0.360 g, 0.0218 mmol) was solubilized in 10 mL of water/ethanol (3:2, v/v) and TCEP (0.0063 g, 0.0218 mmol) was added. After 30 min of stirring at 4 °C under nitrogen atmosphere, the copolymer solution was added to a solution of HA-maleimide (0.124 mmol) in 40 mL of PBS/ethanol (3:2, v/v), to perform the coupling reaction via Michael addition, as previously described²⁷.

To prepare the HA-maleimide derivative, HA (0.065 g, 0.162 mmol) was dissolved in 31.5 mL of a water/ethanol mixture (2:1, v/v) and sodium chloride (0.257 g, 7.24 mmol) was added. Next, aminoethylmaleimide hydrochloride (0.068 g, 0.385 mmol), sulfo-NHS (0.070 g, 0.324 mmol) and EDC (0.124 g, 0.65 mmol) were added and the pH of the solution was maintained between 4.5 and 5 until no further change of pH was observed (\approx 4 h). The resulting product was purified by diafiltration using a membrane Amicon Ultracel MWCO 10 KDa and recovered in pure water (24 mL). Then, PBS 0.1 M (10-fold concentrated) (2.4 mL) was added, followed by immediately adjusting the pH to 4.5. Finally, the copolymer solution was added to the HA-maleimide solution (0.050 g in 18.5 mL, 0.124 mmol) and the reaction mixture was stirred at 4 °C for 4 h. The remaining maleimide units were then converted to carboxylic acid derivatives by addition of excess MPA (42.5 μ L, 0.49 mmol). After stirring for 6 h, the

HA-poly(DMA-co-DAAM) derivative was purified via a batch ion exchange process using DEAE Sepharose CL-6B as a weak-anion exchanger. Briefly, DEAE resin (20 mL), stored in a solution of ethanol 30 %, was washed three times with ultrapure water at 4 °C (3 × 20 mL, contact times of 10 min). Excess liquid was removed by centrifugation (10000 rpm, 10 min) at 4° C. Then, the resin was activated by successive washes with a 0.5 M NaCl aqueous solution (20 mL), a 1 M NaCl aqueous solution (20 mL) and finally, four times with ultrapure water (4 × 20 mL). The HA-poly(DMA-co-DAAM) derivative was then added to the resin in a conical tube and allowed to interact with the resin overnight at 4°C under stirring with an orbital shaker. Then, the HA-derivative bound to the resin was subjected to four washes with ultrapure water (4 × 20 mL) to remove non-grafted copolymer. Finally, the HA-derivative was eluted with a 1 M NaCl aqueous solution (4 × 10 mL). After filtration of the solutions of the recovered HA derivative through a Buchner funnel containing a porous glass filter plate (porosity 4), the solution was dialyzed against deionized water using a dialysis membrane MWCO 100 KDa for 48 h. The product was recovered by freeze-drying as a white powder.

Determination of the poly(DAAM-co-DMA) content in HA-m-poly(DAAM-co-DMA) samples by the carbazole reaction. The degree of substitution (DS), defined as the average number of copolymer units per repeating disaccharide unit, was indirectly determined by reaction of D-glucuronic acid units of HA with carbazole²⁸. Briefly, 800 µL of 25 mM sodium tetraborate solution in sulfuric acid was added to an aqueous solution of HA-m-poly(DAAM-co-DMA) (200 µL) at a concentration of 0.34 g/L. After heating at 100 °C for 10 min, the solution was cooled at room temperature for 15 min, and then a solution of carbazole (200 µL) in absolute ethanol 0.125 % (m/v) was added. The sample was heated again at 100 °C for 10 min and its absorbance was determined by spectrophotometry at 530 nm. The HA concentration was calculated from a calibration curve (0.050 to 0.250 g/L), which allowed the indirect determination of the copolymer amount in the HA-m-poly(DAAM-co-DMA) sample.

Nanogel crosslinking. To a solution of HA-m-poly(DMA-co-DAAM) (0.005 g, 0.0026 mmol) with a DS of 0.1 at a concentration of 1 g/L in PBS (pH 7.4) at room temperature, a solution of isophthalic acid dihydrazide in DMSO (0.073 g/mL) was added under stirring. The volume of the IDH solution (20, 40 and 60 µL) was varied to

obtain IDH/ketone molar ratios of 0.5, 1.0 and 1.5, respectively. Next, the temperature of the solution was increased to 40 °C. After stirring at 40 °C for 24 h, the nanogels suspension was transferred into a dialysis bag (MWCO = 6-8000 Da) and dialyzed against deionized water for 48 h. The core cross-linked nanogels were recovered by freeze-drying.

Labelling of crosslinked nanogels based on HA-m-poly(DAAM-co-DMA) with cyanine 5 and cyanine 5.5. Fluorescent nanogels were obtained by grafting the dye Cy5-amine or Cy5.5-amine on crosslinked nanogels based on HA-m-poly(DAAM-co-DMA) (DS= 0.1) by an amine-acid coupling reaction using DMTMM as a coupling agent²⁹. To this end, crosslinked nanogels (0.010 g, 0.0052 mmol) were solubilized in water/DMF (1:1 v/v; 4 mL) and DMTMM (1.467 mg, 0.0052 mmol) was added to the solution, followed by adjusting the pH to 6.5. After 30 min of stirring, Cy5-amine (0.086 mg, 0.00013 mmol) or Cy5.5-amine (0.099 mg, 0.00013 mmol) solubilized in water/DMF (1:1 v/v) at a concentration of 1 g/L was added to the reaction mixture. After stirring at room temperature for 48 h, the nanogels were purified by dialysis using a membrane MWCO 6-8 KDa against deionized water for 48 h and recovered by freeze-drying.

Scanning electron microscopy. Drops of crosslinked nanogels solutions (0.5 mg/mL) in pure water at both 5 and 40 °C were deposited onto mica-coated copper stubs (also precooled/heated at 5 or 40 °C, respectively) and allowed to air drying at 4 or 40 °C. The samples were then coated by approximately 2 nm of sputtered Au-Pd and observed in secondary electron imaging mode with a ZEISS Ultra 55 FEG-SEM (Grenoble INP - CMTC). Images were acquired at low voltage of 3 kV using an in-lens detector.

Cryo-Transmission Electron Microscopy (Cryo-TEM). Cryo-TEM samples were prepared with an automated vitrification system (Vitrobot Mark IV, FEI, The Netherlands). Crosslinked nanogels solutions (5 mg ml⁻¹) was placed on Lacey carbon grids (TedPella Inc, California, USA) charged previously by glow discharge with 15 mA for 10 seconds in air atmosphere to make them hydrophilic (Pelco easiGlow). Specimens were prepared in a controlled environment with the temperature and humidity set to 22°C for 5 °C sample and 37 °C and 100 % for humidity, respectively,

which prevented sample evaporation sample during the preparation. A 3 μL sample droplet was deposited on a 300 mesh lacey carbon-coated cooper grid (Ted Pella). The excess fluid was blotted off to create an ultra-thin layer, which spans the holes of the support film of the solutions, and prepared with blot force of approximately -5, blot wait of 20 seconds and blot time of 3 seconds of waiting time before blotting. The prepared samples were immediately vitrified by propelling the grids into liquid ethane at its freezing point (-184 $^{\circ}\text{C}$). The vitrified sample grids were transferred under liquid nitrogen by the use of a Gatan (Pleasanton, CA, USA) cryo-holder (Model 626) into a JEOL JEM-1400 plus TEM (Jeol, USA) equipped with FEG and operated at 120 kV acceleration voltage. Microscopy was carried out at -175 $^{\circ}\text{C}$ sample temperature with a defocus range of -2 to -4 μm . Images were acquired using an F-416 CMOS camera (TVIPS, Germany). Sample preparation and data acquisition were performed at the Electron Microscopy Laboratory (LME)/Brazilian Nanotechnology National Laboratory (LNNano).

Hydrophobic drug loading of the nanogels. To 1 mL solution of HA-poly(DMA-co-DAAM) (0.5 g/L in PBS) at room temperature, 15 μL of a solution of PTX in ethanol (1 mg/mL) or 37.5 μL of a solution di-styrylbenzene derivative (DSB) in acetone (0.4 mg/mL) was added. The mixtures were stirred in a water bath at 40 $^{\circ}\text{C}$ for 2 h and solvents was allowed to evaporate slowly. The nanogels suspensions were then filtered at 40 $^{\circ}\text{C}$ through a 1.2 μm polycarbonate filter to eliminate unbound drugs. The amount of PTX entrapped in the nanogels was determined by high-performance liquid chromatography (HPLC) of PTX loaded nanogels after freeze-drying of the nanogels solution and extraction of PTX from nanogels with acetonitrile. Isocratic reverse-phase HPLC was performed using a Nucleodur C18 column at 25 $^{\circ}\text{C}$. The mobile phase consisted of acetonitrile/water (45:55, v/v) with a flow rate of 0.9 mL/min. The signals were recorded UV detector at 227 nm. A calibration curve was established to determine the PTX concentration in the range of 0.5-200 μM , and the r^2 -value of peak area against PTX concentration was at least 0.999. The encapsulation efficiency (EE) was calculated based on the following equation :

$$\text{EE (\%)} = (\text{weight of PTX in nanogels} / \text{weight of the feeding PTX}) \times 100 \%$$

$$\text{DL (\%)} = [\text{recovered PTX mass} / (\text{recovered PTX mass} + \text{HA derivative mass})] \times 100$$

Cell culture. Human cervical cancer cells (HeLa cells) were obtained from American Type Tissue Culture (ATCC, Maryland) and cultured in DMEM supplemented with 10% heat-inactivated FBS, 2 mM L-glutamine, 1 mM sodium pyruvate, 1% penicillin and 1% streptomycin, at 37 °C under a humidified atmosphere containing 5% CO₂. TS/A-pc is an aggressive and poorly immunogenic cell line established from the first *in vivo* transplant of a moderately differentiated mammary adenocarcinoma that arose spontaneously in a 20- month-old multiparous BALB/c mouse. TS/A-pc cells were cultured in RPMI 1640 medium supplemented with 10% FCS, L-glutamine (200 mmol/l), penicillin (10,000 IU/ml) and streptomycin (10,000 µg mL⁻¹). The cells were maintained at 37°C in 95% air/5% CO₂. When ~ 90% confluence was reached, the culture medium was removed and replaced by FCS-free medium. The cells were detached mechanically and counted under the microscope. They were then centrifuged (5 min, 200 g) and the pellet was resuspended in sterile NaCl 0.9% for extemporaneous administration to the animals.

***In Vitro* cytotoxicity Assays.** *In vitro* cytotoxicity of PTX-loaded and PTX-free crosslinked nanogels, Genexol-PM (Samyang Biopharmaceuticals), initial HA, the HA-maleimide intermediate, PTX mixed with initial HA and PTX mixed with the HA-maleimide intermediate was evaluated by MTT assay with HeLa and TS/A pc cells as previously described³⁰. Cells were seeded into 96-well plates (10000 cells per well, suspended in 200 µL of culture medium) and incubated for 24 h. Then, cells were incubated with PTX-loaded and PTX-free crosslinked nanogels, Genexol-PM, initial HA, the HA-maleimide intermediate, PTX mixed with initial HA and PTX mixed with the HA-maleimide intermediate at 37 °C for 72 h. Subsequently, the culture medium was removed and the cells were washed with 250 µL of PBS. Finally, 100 µL of MTT solution (prepared by dissolving 100 mg of MTT in 20 mL of PBS and subsequent membrane filtration (0.22 µm)) was added and the cells were incubated for 2.5 h. Finally, the MTT working solution was removed and the formed purple formazan crystals were dissolved in 50 µL of DMSO. Absorbance was determined at 590 nm using an EnVision Multilabel plate reader. The absorbance of the positive control was used as a blank and therefore subtracted from all values. Cell viability (%) was calculated according to the equation below. All experiments were run three times.

$$\text{Cell viability (\%)} = \frac{\text{Abs(test cell)} - \text{Abs(background)}}{\text{Abs(controlled cell)} - \text{Abs(background)}} \times 100 \%$$

Cellular uptake of nanogels by HeLa and TS/a-pc cells. HeLa and TS/a-pc cells were plated in 8-wells LabTek Dishes (2.5×10^5 cells mL^{-1} in 200 μL of DMEM medium) and cultured for 8 h at 37 °C and 5% CO_2 . Uptake experiments were then performed by incubating cells during ~16 h with Cyanine 5-labelled crosslinked nanogels solution (250 $\mu\text{g}/\text{mL}$) (empty or loaded with DSB) at 37 °C and 5 % CO_2 . After fixation in 4% paraformaldehyde, cells were stained with Hoechst (10 μL of a 1 mg/mL stock in DMSO) for 40 min at room temperature. Microscopy images were recorded on a Leica DMI 6000 microscope coupled to an Andor DSD2 scanner and a Zyla5.5 CMOS camera. Images were processed with the ImageJ software package.

***In vivo* biodistribution.** The *in vivo* behavior of crosslinked nanogels was tested in *nude* mice bearing TS/a-pc xenografts in their right flank ($n = 3$). Female NMRI *nude* mice (6–8 weeks, Janvier, Le Genest-Saint-Isle, France) were injected subcutaneously with 1×10^7 TS/a-pc cells per mouse. After tumor growth (6 weeks), anesthetized mice (isoflurane/oxygen 3.5/4% for induction and 1.5/2% thereafter; CSP, Cournon, France) were injected in the tail vein with 100 μl of a dispersion of Cyanine 5.5-labelled crosslinked nanogel (3 mg/ml in PBS). Fluorescence images were acquired by a back-thinned CCD camera (ORCAII-BT-512G, Hamamatsu, Massy, France) after 30 min, 1 h, 2 h30, 5 h, 24 h and 48 h of the injection. After the imaging, at 24 h and 48 h, the mice were sacrificed and dissected in order to image the organs and analyze the blood. Image display and analysis were performed using Wasabi software (Hamamatsu, Massy, France). Semi-quantitative data were obtained by drawing regions of interest (ROI) around each organ. All procedures and experimental protocols were approved by the ethical committee of Grenoble (France) for the use of animal research.

3. Results and Discussion

3.1. Synthesis and characterization of core-crosslinked nanogels.

To prepare core-crosslinked nanogels, our approach was to functionalize HA with a thermosensitive ketone-containing copolymer prepared from diacetone

acrylamide (DAAM) and *N,N*-dimethylacrylamide (DMA) as illustrated in Figure 1. DAAM is not only interesting as a crosslinkable group but also as a hydrophobic comonomer of DMA, which allows to prepare copolymers exhibiting a lower critical solution temperature (LCST) below body temperature²². DAAM and DMA were copolymerized by RAFT polymerization using 2,2'-azobis(2-methylpropionitrile) (AIBN) as an initiator and 2-(butylthiocarbonothioylthio)propanoic acid (PABTC) as a chain transfer agent (CTA). The molar ratio of monomers:CTA was fixed at 100:1 with a DAAM/DMA feed ratio of 75:25. The obtained copolymer displayed a low dispersity (\mathcal{D}) value (1.1) with a number average molar mass M_n of 16.45 kg/mol. ¹H-NMR analysis revealed a final copolymer composition DAAM/DMA of 57:33 indicating the preferential incorporation of the more reactive DMA monomer within the copolymer, as previously reported²² (Figure SI-1). The copolymer exhibited a cloud point temperature (T_{cp}) of 24 °C (Figure SI-2). Subsequently, poly(DAAM-co-DMA) of which the RAFT trithiocarbonate end-group was converted to a free thiol by aminolysis using *n*-butylamine was grafted onto HA ($M_w = 40$ kg/mol) containing maleimide moieties by formation of a thioether bond²⁷ (Figure 1).

After conversion of the remaining maleimide units to carboxylic acid derivatives by addition of an excess of mercaptopropionic acid, the HA-m-poly(DAAM-co-DMA) conjugate was purified via a batch ion exchange process, and finally dialyzed. The structural integrity of the HA-m-poly(DAAM-co-DMA) was ascertained by ¹H NMR analysis (Figure 2). The degree of substitution (DS) of the conjugate, determined by the carbazole assay,²⁸ was found to be 0.10.

Nanogels were obtained by heating solutions of HA-m-poly(DAAM-co-DMA) in PBS (pH 7.4) above its critical aggregation temperature (CAT) which was found to be 32 °C. This was determined by measuring the light scattering intensity of a solution of the HA derivative in PBS (0.5 g/L) as a function of temperature (Figure SI-3). The higher value of the CAT compared to the T_{cp} of the copolymer poly(DAAM-co-DMA) can be related to the presence of the highly hydrophilic and negatively charged HA backbone. Dynamic light scattering (DLS) measurements at 40 °C showed that the nanogels had a hydrodynamic diameter around 147 nm with a low polydispersity index of 0.11 (Table 1).

Table 1. Size and polydispersity of nanogels based on HA-m-poly(DAAM-co-DMA) determined by dynamic light scattering (0.5 g/L in PBS).

	18 °C		40 °C	
	Diameter ^a (nm)	PDI	Diameter (nm) ^a	PDI
Non-crosslinked nanogel	-- ^b	-- ^b	147.5 ± 51.80	0.114
Crosslinked nanogels (0.5 equiv. IDH)	307.3 ± 122.3	0.149	157.8 ± 58.10	0.098

^aDiameter by volume; ^bno nanogel formation

The resulting nanogels were then crosslinked by reaction of the keto-functional copolymer chains with a bifunctional dihydrazide, namely isophthalic dihydrazide (IDH) in aqueous medium as shown in Scheme 1. After core-crosslinking using a IDH to ketone molar ratio of 0.5, the nanogel structure became “frozen” and remained stable at low temperature (below the T_{cp} of the copolymer) as demonstrated by DLS measurements and microscopy observations (Figure 3). The cryo-TEM and SEM images of nanogel suspensions vitrified and dried at 5 °C revealed the presence of nanogels at low temperature (Figure 3C and 3E). In accordance to the DLS data (Table 1 and Figure 3B), the nanogels at 40 °C observed by cryo-TEM had a diameter below 200 nm (Figure 3D). The nanogels at 5 °C had a diameter around 200 nm (Figure 3C). This is in line with DLS analysis which indicated an increase of the average diameter of the nanogels from 147 to 307 nm by lowering the temperature from 40 to 18 °C (Table 1). The larger size of the nanogels at 18 and 5 °C can be attributed to increased hydration of the crosslinked copolymer chains, resulting in the nanogel swelling. In the SEM images, the size of the nanogels appeared to be much smaller due to shrinkage during drying.

In the next step, we varied the IDH to ketone molar ratio from 0.5 to 1.5 in the crosslinking step to ensure that all nanogels were sufficiently crosslinked to be stable at low temperature. The SEM images obtained from crosslinked nanogel suspensions at 5 °C suggested a slightly lower amount of nanogels crosslinked using a IDH to ketone molar ratio of 0.5 (Figure 4).

This was confirmed by static light scattering experiments performed on the non-crosslinked and crosslinked nanogels (Figure 5). The non-crosslinked nanogels showed a continuous decrease of the light scattering intensity (LSI) from 40 to 15 °C, indicating gradual disassembly of the nanogels due to hydration of the thermosensitive copolymer chains. The LSI of the nanogels crosslinked with 0.5 molar equiv. of IDH slightly decreased upon cooling, suggesting dissociation of some nanogels. In contrast, the LSI of the nanogels crosslinked with 1 and 1.5 molar equiv. of IDH was constant upon cooling, demonstrating efficient nanogel crosslinking. These results also indicate that the crosslinking density can be tuned by varying the degree of dihydrazide to diacetone monomer molar ratio. Compared to strategies previously used for covalently crosslinking self-assembled nanoparticles based on HA,¹⁴ this strategy based on keto-hydrazide chemistry has the advantage of controlling efficiently the extent of crosslinking.

Paclitaxel (PTX), a commonly used chemotherapeutic agent for the treatment of various cancers, was physically loaded into the nanogels before and after their crosslinking via addition of IDH. Interestingly, the crosslinking before loading neither inhibited the loading procedure, nor significantly reduced the encapsulation efficiency of PTX (Table 2).

Table 2. Encapsulation efficiency (EE) and drug loading (DL) of PTX-loaded HA-m-poly(DAAM-co-DMA) nanogels in PBS (1 g/L).

Nanogels	EE (%)	DL (%)
Non-crosslinked	35.9 ± 9.7	0.47 ± 0.1
Crosslinked nanogels ^a	32.2 ± 8.4	0.42 ± 0.1

^aCrosslinking with 0.5 equiv. IDH

3.2. Cellular uptake and cytotoxicity of nanogels based on HA-m-poly(DAAM-co-DMA).

The *in vitro* antitumor activity of PTX-loaded nanogels was evaluated in HeLa cells (human cervical cancer cells), which overexpress HA-binding CD44 receptors,³¹⁻³³

and TS/A-pc (parent TS/A cells) by MTT assays. The cytotoxicity experiments were performed using nanogels crosslinked with a IDH to ketone molar ratio of 0.5. Indeed, it was found that non-crosslinked HA-m-poly(DAAM-co-DMA) was not stable upon long-term storage, as revealed by difficulties in perfectly solubilizing the product in aqueous solution after lyophilization. This may be due to side reactions involving ketone functional groups though they are more stable than aldehydes. The cytotoxicity studies showed that the crosslinked nanogels were highly potent against HeLa cells (Figure 6A). It is interesting to note that the potency of PTX-loaded crosslinked nanogels was similar to that of the clinically used PTX nanoformulation based on polymeric micelles, Genexol-PM^{30, 34}. In contrast, native HA, the HA-maleimide intermediate and crosslinked nanogels without PTX did not significantly alter HeLa cell viability, which implies that the cytocompatibility of HA was not significantly affected via chemical modification. Regarding the TS/A-pc, the cytotoxicity tests revealed that the crosslinked nanogels loaded with PTX as well as Genexol-PM showed low cytotoxic potency (Figure 6B). The cell viability (CV) after incubation with Genexol-PM and the nanogels with a PTX concentration of 0.1 $\mu\text{g/mL}$ was 78 %, whereas the CV was nearly 0 % for HeLa cells with the same PTX concentration. The difference in the cytotoxicity of these cell lines may be attributed to their different sensitivity to PTX, based on the results obtained with Genexol-PM.

In order to investigate the cellular uptake of the nanogels and intracellular drug release, the crosslinked nanogels were labeled with cyanine 5 and loaded with a fluorescent di-strylbenzene derivative³⁵ (DSB) as a model hydrophobic drug. After incubation overnight (≈ 16 h) of HeLa cells with empty nanogels, confocal microscopy analysis showed red fluorescence signals from the nanogels in the cytoplasm, indicating that the nanogels were well-internalized into HeLa cells probably via a HA-induced endocytosis mechanism (Figure 7A). Several studies previously reported efficient internalization of HA-based nanoparticles by these cells via a HA-induced endocytosis mechanism³¹⁻³³. It was also possible to see green spots of fluorescence (Figure 7B) corresponding to DSB molecules, indicating that the nanogels could not only efficiently carry their hydrophobic cargo, but also deliver it into the intracellular environment. Indeed, the only partial intracellular colocalization of the fluorescent nanogels with DSB suggests a separation between carrier and cargo after cellular uptake.

It should be noted that when HeLa cells were incubated with filtered and unfiltered native HA solutions containing free DSB, a very low cellular uptake of the free dye was observed³⁶. Separation between drug and carrier after internalization may thus be related to degradation of HA by hyaluronidase overexpressed mainly in the cytoplasm of cancer cells, which was shown in the case of HeLa cells^{31, 32}. These data demonstrated the ability of our nanogels to efficiently carry hydrophobic molecules to the intracellular environment. However, for TS/A pc cells, Cy5-labeled crosslinked nanogels (Figure 7C) were only partly internalized after overnight incubation. Indeed, significant red fluorescence signal could be observed on the cell surface. Similarly to HeLa cells, the green spots of fluorescence corresponding to DSB inside cells correlates with the ability of the nanogels to deliver their hydrophobic cargo once internalized (Figure 7D). These results are in line with those obtained from the cytotoxicity experiments showing that PTX can still keep its pharmacological activity when encapsulated into nanogels, but that the inhibition of the cell proliferation is related to the cell type.

3.3. *In vivo* biodistribution of Cy5.5-labeled nanogels based on HA-m-poly(DAAM-co-DMA).

The *in vivo* biodistribution and tumor localization of crosslinked nanogels (with 0.5 equiv. IDH) labeled with Cy5.5 were assessed using full body *in vivo* fluorescence imaging following intravenous injection in breast (TS/A-pc) tumor-bearing mice (Figure 8).

These data show that the fluorescence intensity in the tumor gradually increased up to 24 h. This indicated that nanogels could circulate for a long period of time in the body and continuously accumulate at the tumor site. Tumors also maintained strong fluorescence intensity for two days as seen from the quantitative analyses (figure 8B and 8C). Tumor site accumulation could be attributed to the highly permeable vascular structure of the neoplasm, which always leads to a passive accumulation of nanosized materials (EPR effect)^{37, 38}.

In addition to the site of the tumor, fluorescence could also be detected in other organs to various extents (Figure 8C), with liver and spleen exhibiting the highest nanogel accumulation. This accumulation may be due to cellular uptake of the nanogels

by phagocytic cells of the reticuloendothelial system and by cells expressing HARE receptors which are abundant in the site.^{13, 39} It is also known that the liver is the major organ that uptakes and accumulates any types of nano/micro particles⁴⁰. Collectively, these results suggest that crosslinked nanogels exhibit enhanced tumor uptake and improved biodistribution even after 48 h post-injection.

4. Conclusions

In this study, novel biocompatible and biodegradable nanogels were fabricated from hyaluronic acid modified with a ketone-functional copolymer. The nanogels are prepared by a simple method based on the temperature-triggered assembly of the HA conjugate followed by crosslinking the hydrophobic nanodomains of the copolymer chains by hydrazone formation. These cross-links throughout the hydrophobic domains in the core of the nanogels affect neither the encapsulation efficiency of the particles nor the properties of the hydrophilic shell. In addition their density can be tuned by varying the dihydrazide crosslinker to ketone group molar ratio. *In vitro* biological studies revealed that the empty nanogels have low cytotoxicity against cancer cells. It was further shown that the anticancer drug PTX can be entrapped into the nanogels and be delivered intracellularly in CD44-positive HeLa cancer cells, resulting in their eradication with high efficiency. Finally *in vivo* studies demonstrated that following intravenous administration in tumor-bearing mice, the crosslinked nanogels were able to circulate in the bloodstream and accumulate in the tumor tissue. These results suggest that these nanogels hold great potential as nanocarriers for the delivery of chemotherapeutics in anti-cancer therapy.

Corresponding Author

Rachel Auzèly-Velty

Tel: +33 4 76 03 76 71. E-mail: rachel.auzely@cermav.cnrs.fr

Author Contributions

The manuscript was written through contributions of all authors. All authors have given approval to the final version of the manuscript.

Funding Sources

The authors thank the “Conselho Nacional de Desenvolvimento Científico e Tecnológico- Conselho Nacional de Desenvolvimento Científico e Tecnológico (CNPq)” for financial support to this work. F.P.G. gratefully acknowledges the “Science Without Borders Program” of CNPq for the sandwich doctorate scholarship. This work was also partly supported by the “Agence Nationale pour la Recherche” (grant ANR-14-CE08-0014-01 for the “OPENER” project) as well as in the framework of the Glyco@Alps project of the "Investissements d'avenir" program (ANR-15-IDEX-02). This work was also supported through grants from the Capacitação de Aperfeiçoamento de Pessoal de Nível Superior (CAPES) and Financiadora de Estudos e Projetos (FINEP).

ACKNOWLEDGMENT

The authors thank LME/LNNano as well as Dr. Rodrigo Portugal and Dr. Alexandre Cassago for the use of electron microscopy facility and technical support; Francine Roussel-Dherbey at Grenoble INP-CMTC for her help with SEM observations; the NMR platform of ICMG (FR2607) for its support. They gratefully acknowledge O. Stephan at LIphy (Grenoble), who kindly provided DSB.

ABBREVIATIONS

HA, Hyaluronic acid; Cy5.5, cyanine5.5 amine; Cy5, cyanine5 amine; DAAM, diacetone acrylamide; DMA, *N,N*-dimethylacrylamide; IDH, isophtalic dihydrazide; AIBN, 2,2-azobis(2-methylpropionitrile); PBS, phosphate buffer saline; TCEP, Tris-(2-carboxyethyl)phosphine hydrochloride; MPA, mercaptopropionic acid; MTT, 3-(4,5-dimethylthiazol-2-yl)-2,5-diphenyltetrazolium bromide; DMF, dimethylformamide; DMSO, dimethylsulfoxide; DMTMM, 4-(4,6-dimethoxy-1,3,5-triazin-2-yl)-4-methylmorpholinium chloride, SulfoNHS, *N*-hydroxysulfosuccinimide sodium salt; EDC, *N*-(3-dimethylaminopropyl)-*N*'-ethylcarbodiimide hydrochloride; PTX, Paclitaxel; DSB, di-strylbenzene derivative; DMEM, Dulbecco's Modified Eagle Medium; FBS, fetal bovine serum; DEAE, diethylaminoethylcellulose resin; PABTC, 2-(Butylthiocarbonothioylthio)propanoic acid; EE, Encapsulation efficiency; DL, drug

loading; SEM, scanning electron microscopy; TEM, transmission electron microscopy; SEC, size exclusion chromatography; LSI, light scattering intensity; DLS, dynamic light scattering; SLS, static light scattering; PDI, polydispersity index; DS, degree of substitution; ^1H NMR, proton nuclear magnetic resonance; RAFT, reversible addition-fragmentation chain transfer; CTA, chain transfer agent; CAT, critical aggregation temperature; T_{cp} , Cloud point temperature; M_n , number average molar mass; M_w , weight average molar mass; D , dispersity; RI, refractive index; D_2O , Deuterium oxide; DMSO- d_6 , dimethylsulfoxide- d_6 .

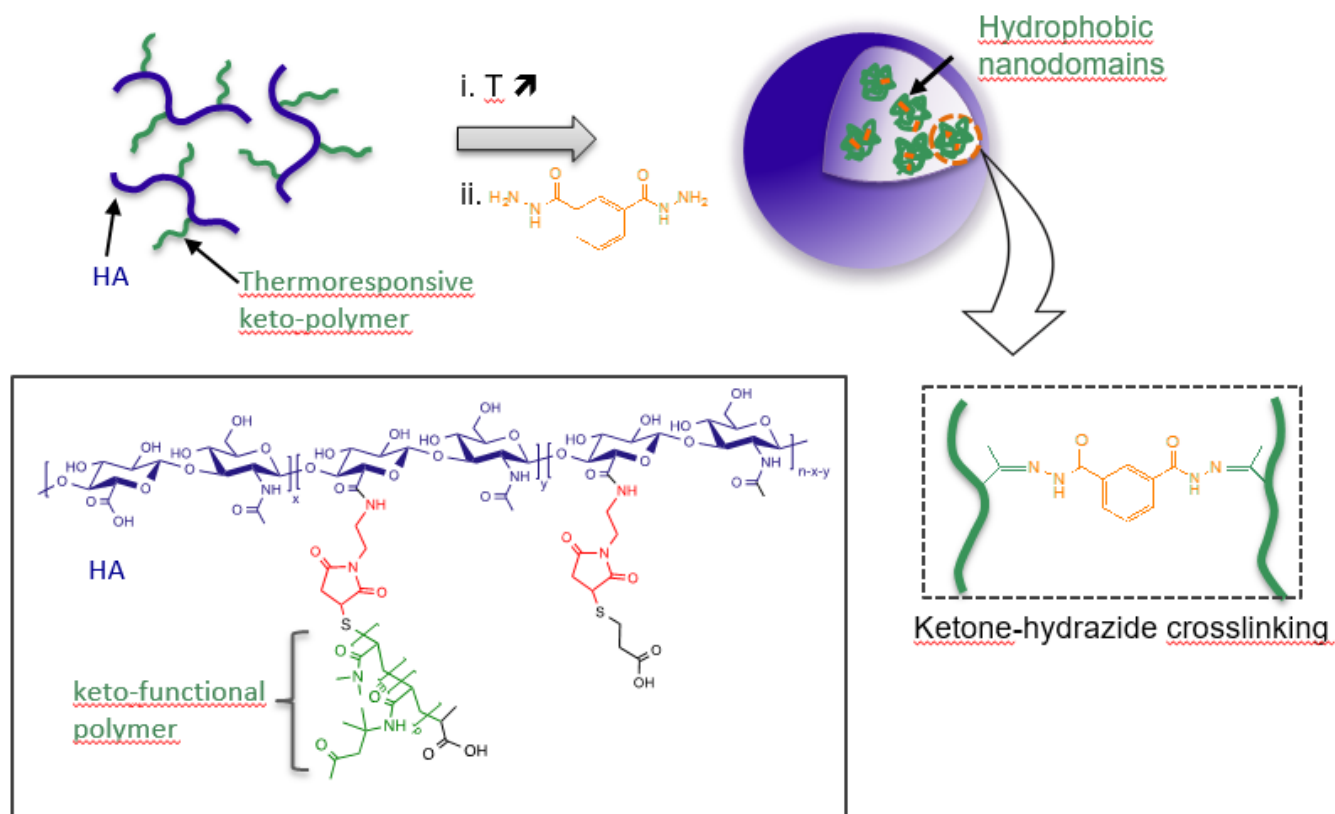
5. REFERENCES

1. A. Debele Tilahun, L. Mekuria Shewaye and H.-C. Tsai, *Mater Sci Eng C Mater Biol Appl*, 2016, **68**, 964.
2. G. Soni and S. Yadav Khushwant, *Saudi Pharm J*, 2016, **24**, 133.
3. H.-Q. Wu and C.-C. Wang, *Langmuir*, 2016, **32**, 6211.
4. M. M. Yallapu, M. Jaggi and S. C. Chauhan, *Drug Discovery Today*, 2011, **16**, 457.
5. Y. H. Bae and H. Yin, *J. Controlled Release*, 2008, **131**, 2.
6. H. Maeda, J. Wu, T. Sawa, Y. Matsumura and K. Hori, *J. Controlled Release*, 2000, **65**, 271.
7. R. K. O'Reilly, C. J. Hawker and K. L. Wooley, *Chem. Soc. Rev.*, 2006, **35**, 1068.
8. E. S. Read and S. P. Armes, *Chem. Commun. (Cambridge, U. K.)*, 2007, DOI: 10.1039/b701217a, 3021.
9. Y. Shao, W. Huang, C. Shi, S. T. Atkinson and J. Luo, *Ther. Delivery*, 2012, **3**, 1409.
10. M. Talelli, M. Barz, C. J. F. Rijcken, F. Kiessling, W. E. Hennink and T. Lammers, *Nano Today*, 2015, **10**, 93.
11. C. F. van Nostrum, *Soft Matter*, 2011, **7**, 3246.
12. A. Cadete and M. J. Alonso, *Nanomedicine (London, U. K.)*, 2016, **11**, 2341.
13. K. Y. Choi, G. Saravanakumar, J. H. Park and K. Park, *Colloids Surf., B*, 2012, **99**, 82.

14. N. V. Rao, H. Y. Yoon, H. S. Han, H. Ko, S. Son, M. Lee, H. Lee, D.-G. Jo, Y. M. Kang and J. H. Park, *Expert Opin. Drug Delivery*, 2016, **13**, 239.
15. S. Banerji, A. J. Wright, M. Noble, D. J. Mahoney, I. D. Campbell, A. J. Day and D. G. Jackson, *Nat. Struct. Mol. Biol.*, 2007, **14**, 234.
16. E. Hachet, H. Van Den Berghe, E. Bayma, M. R. Block and R. Auzely-Velty, *Biomacromolecules*, 2012, **13**, 1818.
17. J. Lesley, V. C. Hascall, M. Tammi and R. Hyman, *J. Biol. Chem.*, 2000, **275**, 26967.
18. G. Jiang, K. Park, J. Kim, K. S. Kim and S. K. Hahn, *Mol. Pharmaceutics*, 2009, **6**, 727.
19. E. J. Oh, K. Park, K. S. Kim, J. Kim, J.-A. Yang, J.-H. Kong, M. Y. Lee, A. S. Hoffman and S. K. Hahn, *J. Controlled Release*, 2010, **141**, 2.
20. Y. Zhong, K. Goltsche, L. Cheng, F. Xie, F. Meng, C. Deng, Z. Zhong and R. Haag, *Biomaterials*, 2016, **84**, 250.
21. Y. Zhong, J. Zhang, R. Cheng, C. Deng, F. Meng, F. Xie and Z. Zhong, *J. Controlled Release*, 2015, **205**, 144.
22. X. Tang, J. Han, Z. Zhu, X. Lu, H. Chen and Y. Cai, *Polym. Chem.*, 2014, **5**, 4115.
23. S. Mukherjee, A. P. Bapat, M. R. Hill and B. S. Sumerlin, *Polym. Chem.*, 2014, **5**, 6923.
24. J. Liu, R. C. Li, G. J. Sand, V. Bulmus, T. P. Davis and H. D. Maynard, *Macromolecules (Washington, DC, U. S.)*, 2013, **46**, 8.
25. W. Zhou, Q. Qu, Y. Xu and Z. An, *ACS Macro Lett.*, 2015, **4**, 495.
26. C. J. Ferguson, R. J. Hughes, D. Nguyen, B. T. T. Pham, R. G. Gilbert, A. K. Serelis, C. H. Such and B. S. Hawkett, *Macromolecules*, 2005, **38**, 2191.
27. J. Jing, D. Alaimo, E. De Vlieghere, C. Jerome, O. De Wever, B. G. De Geest and R. Auzely-Velty, *J. Mater. Chem. B*, 2013, **1**, 3883.
28. M. Cesaretti, E. Luppi, F. Maccari and N. Volpi, *Carbohydr. Polym.*, 2003, **54**, 59.
29. M. D'Este, D. Eglin and M. Alini, *Carbohydr. Polym.*, 2014, **108**, 239.
30. B. Louage, Q. Zhang, N. Vanparijs, L. Voorhaar, S. Vande Castele, Y. Shi, W. E. Hennink, J. Van Bocxlaer, R. Hoogenboom and B. G. De Geest, *Biomacromolecules*, 2015, **16**, 336.

31. Y. Huang, C. Song, H. Li, R. Zhang, R. Jiang, X. Liu, G. Zhang, Q. Fan, L. Wang and W. Huang, *ACS Appl. Mater. Interfaces*, 2015, **7**, 21529.
32. F. Li, B.-c. Bae and K. Na, *Bioconjugate Chem.*, 2010, **21**, 1312.
33. W. Park, K. s. Kim, B.-c. Bae, Y.-H. Kim and K. Na, *Eur. J. Pharm. Sci.*, 2010, **40**, 367.
34. M. A. Moretton, E. Bernabeu, E. Grotz, L. Gonzalez, M. Zubillaga and D. A. Chiappetta, *Eur. J. Pharm. Biopharm.*, 2017, **114**, 305.
35. M. Maurin, L. Vurth, J.-C. Vial, P. Baldeck, S. R. Marder, B. van der Sanden and O. Stephan, *Nanotechnology*, 2009, **20**, 235102/1.
36. S. Arpicco, G. De Rosa and E. Fattal, *J. Drug Delivery*, 2013, DOI: 10.1155/2013/860780, 860780.
37. T. Xing, C. Mao, B. Lai and L. Yan, *ACS Appl. Mater. Interfaces*, 2012, **4**, 5662.
38. Y. Matsumura and H. Maeda, *Cancer Res.*, 1986, **46**, 6387.
39. M. Zheng, S. Kimura, J. Nio-Kobayashi and T. Iwanaga, *Biomed. Res.*, 2016, **37**, 187.
40. J.-Y. Kim, W. I. Choi, Y. H. Kim and G. Tae, *J. Controlled Release*, 2011, **156**, 398.

6. Figures



Scheme 1. Formation of hyaluronic acid-based nanogels by temperature-induced self-assembly and their covalent crosslinking by hydrazone bond formation within the hydrophobic domains of the grafted copolymer chains.

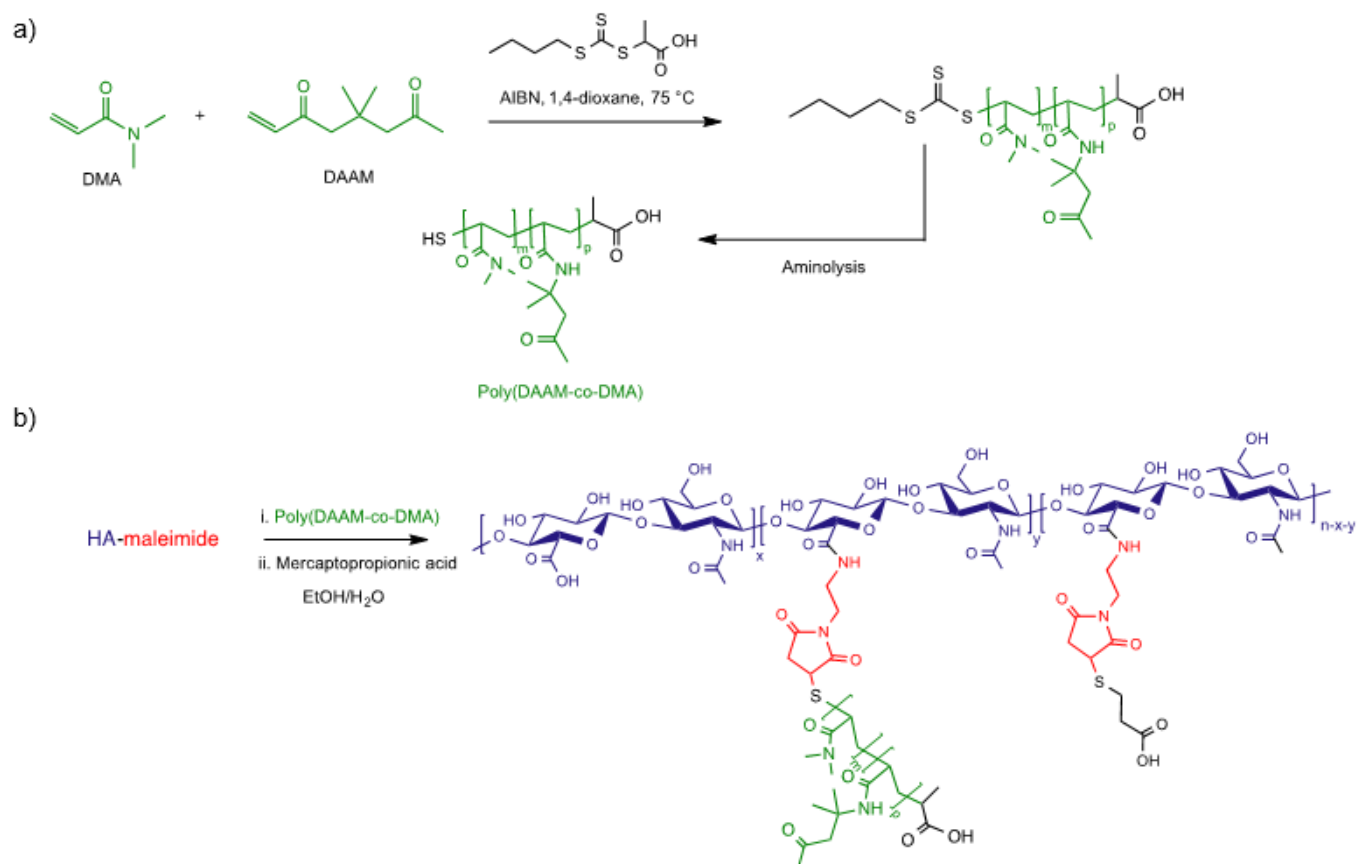


Figure 1. Synthesis of poly(DAAM-co-DMA) and its covalent grafting on hyaluronic acid by a thiol-maleimide coupling reaction.

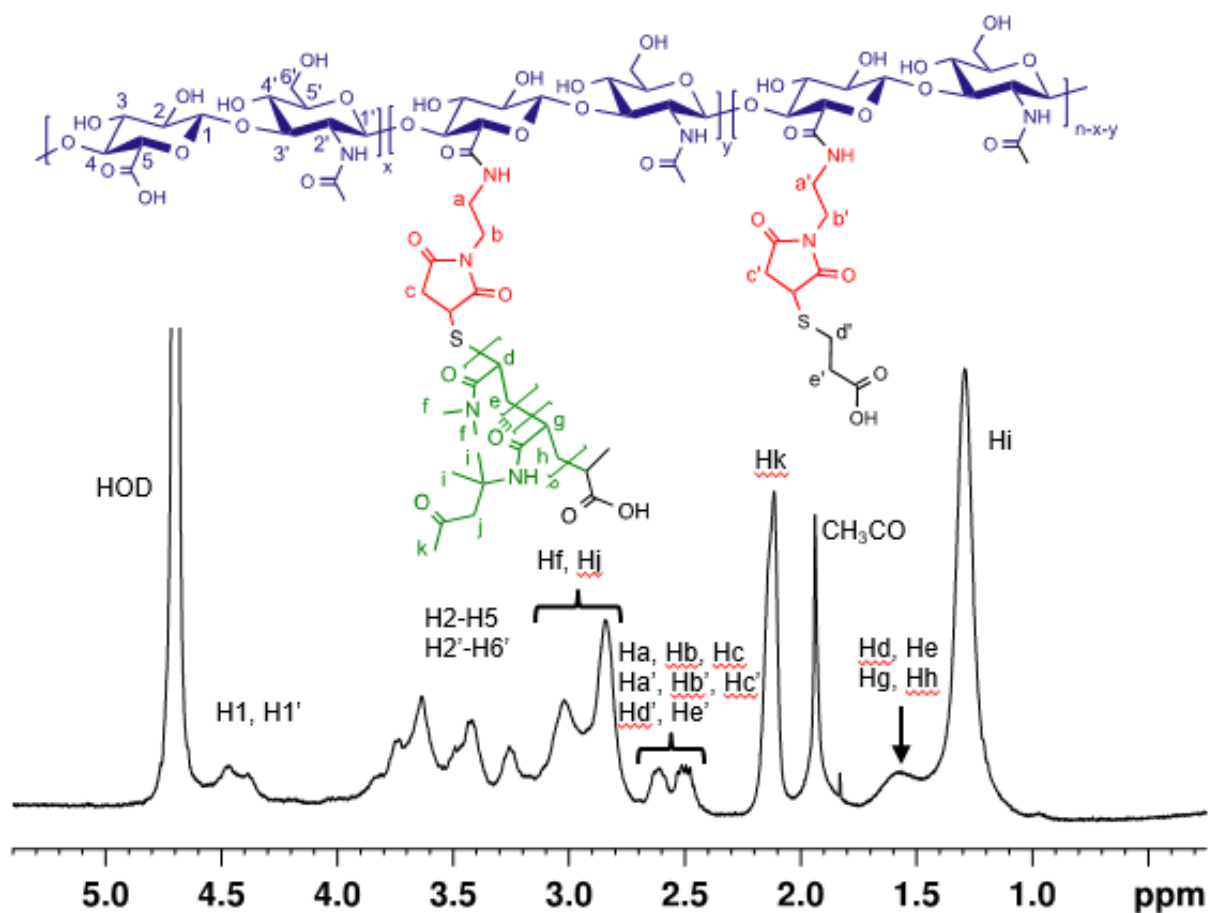


Figure 2. ¹H NMR spectrum (400 MHz, 6 mg/mL in D₂O, 25 °C) of HA-m-poly(DAAM-co-DMA).

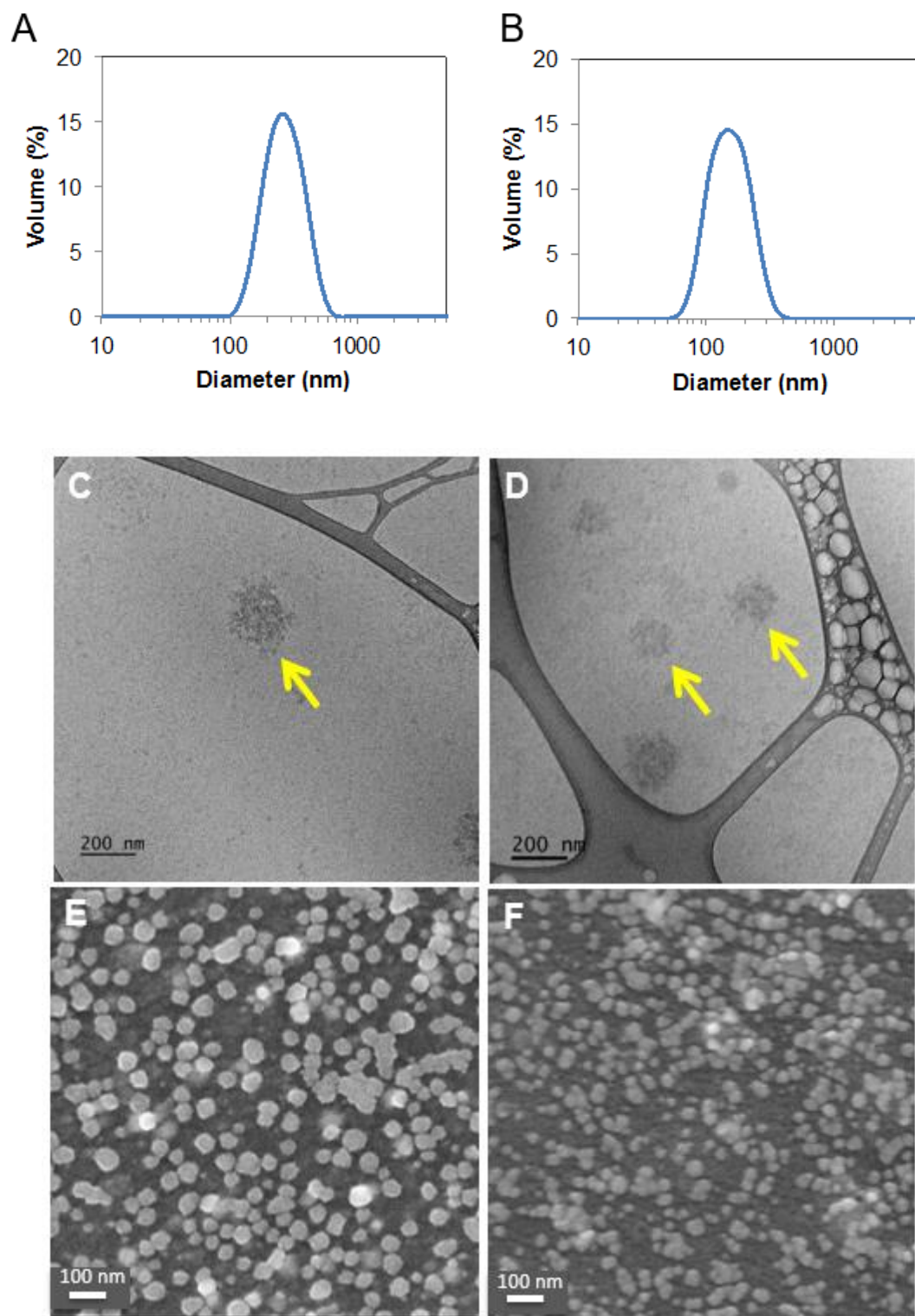


Figure 3. Size distribution of HA-based nanogels crosslinked with a IDH:ketone molar ratio of 0.5 measured by DLS at 18°C (A) and 40 °C (B); morphology observed at 5 °C (C, E) and 40 °C (D, F) by cryo-TEM (C, D) and SEM (E, F).

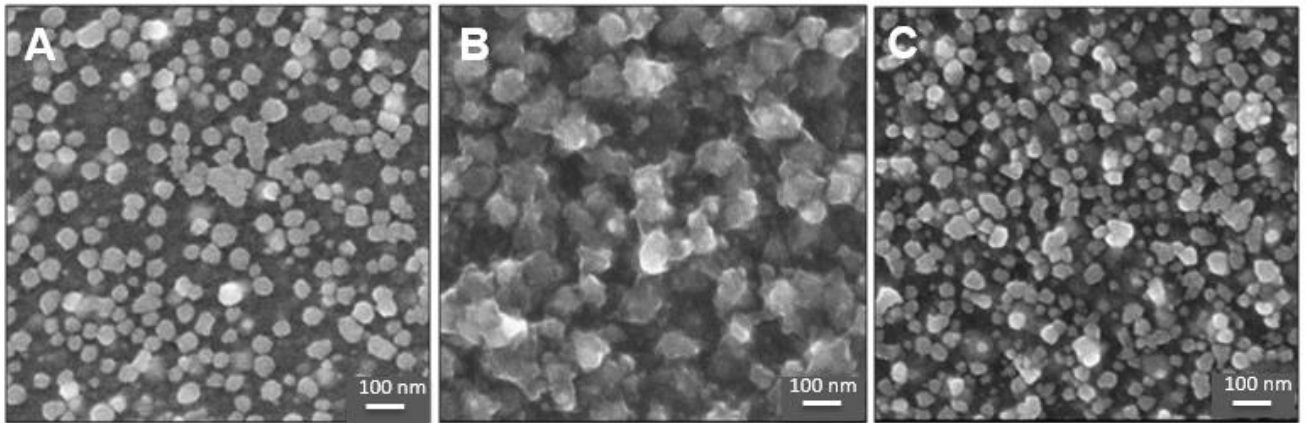


Figure 4. SEM observation at 5 °C of HA-based nanogels crosslinked with IDH to ketone molar ratios of 0.5 (A), 1.0 (B) and 1.5 (C).

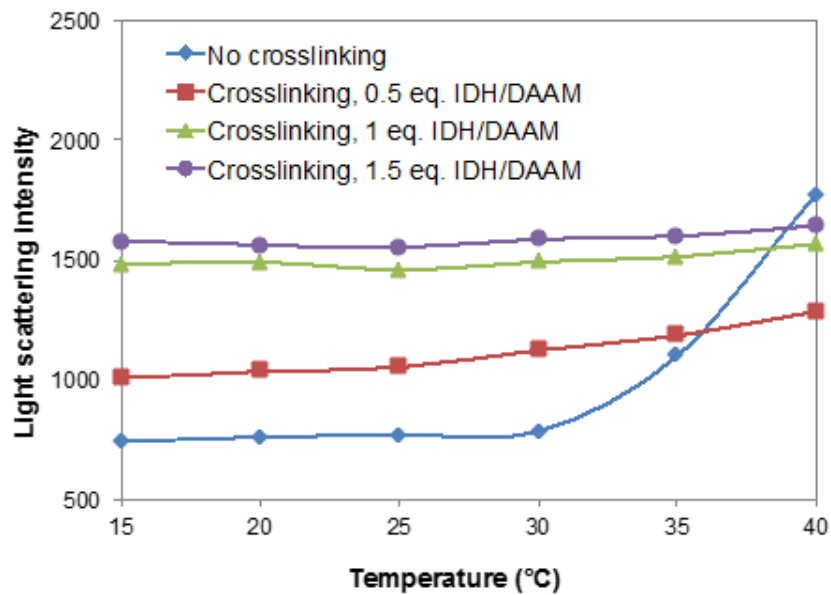


Figure 5. Light scattering intensity of non-crosslinked HA-based nanogels and nanogels crosslinked with IDH to ketone molar ratios of 0.5, 1.0 and 1.5 upon cooling from 40 to 15 °C.

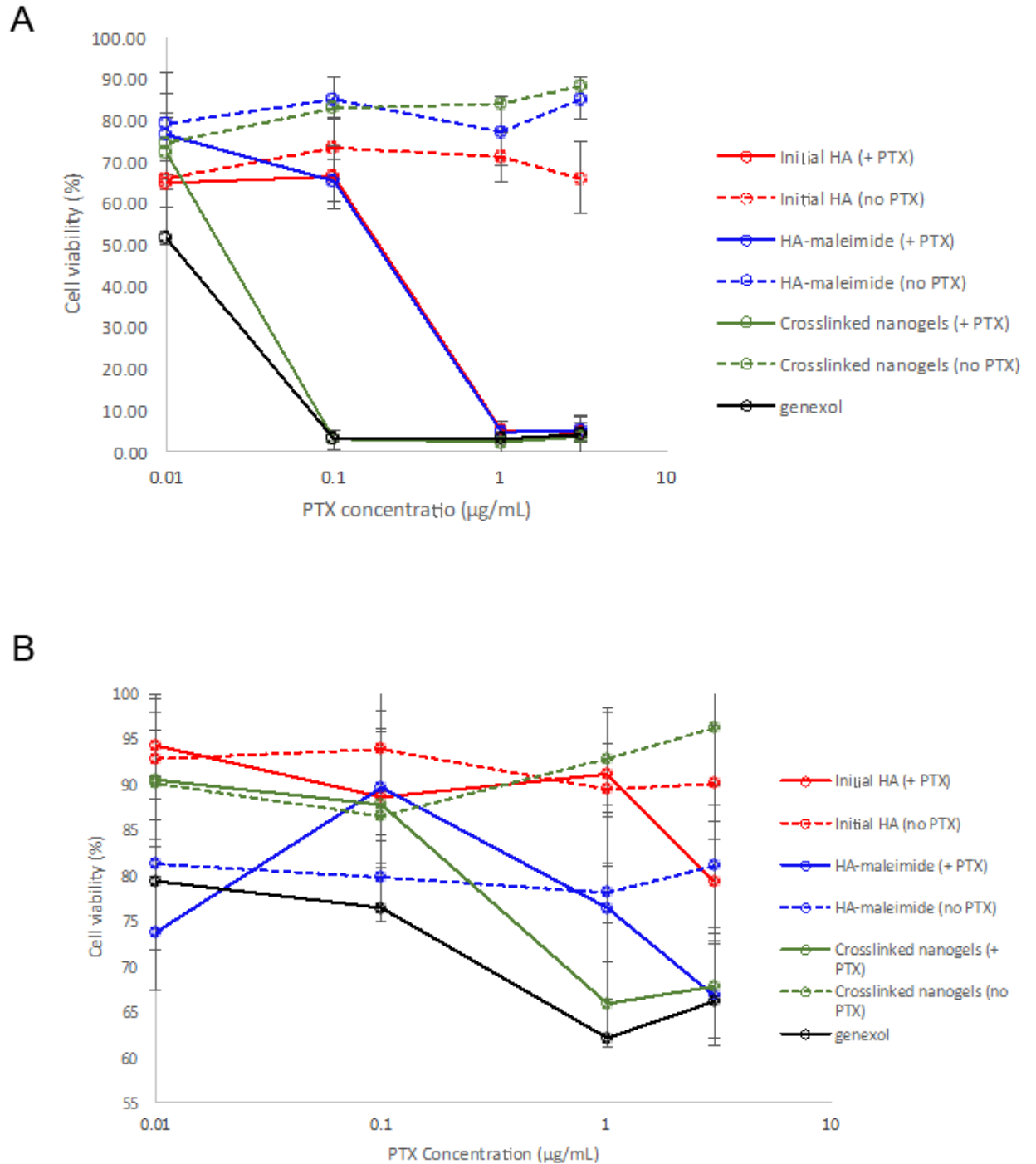


Figure 6. Viability of HeLa cells (A) and TS/A pc cells (B) measured by MTT assay, after incubation for 72 h with initial HA alone and in the presence of PTX; the HA-maleimide intermediate alone and in the presence of PTX; PTX-loaded and PTX-free crosslinked nanogels based on HA as well as with Genexol-PM. Data are represented as mean \pm SD (n = 3).

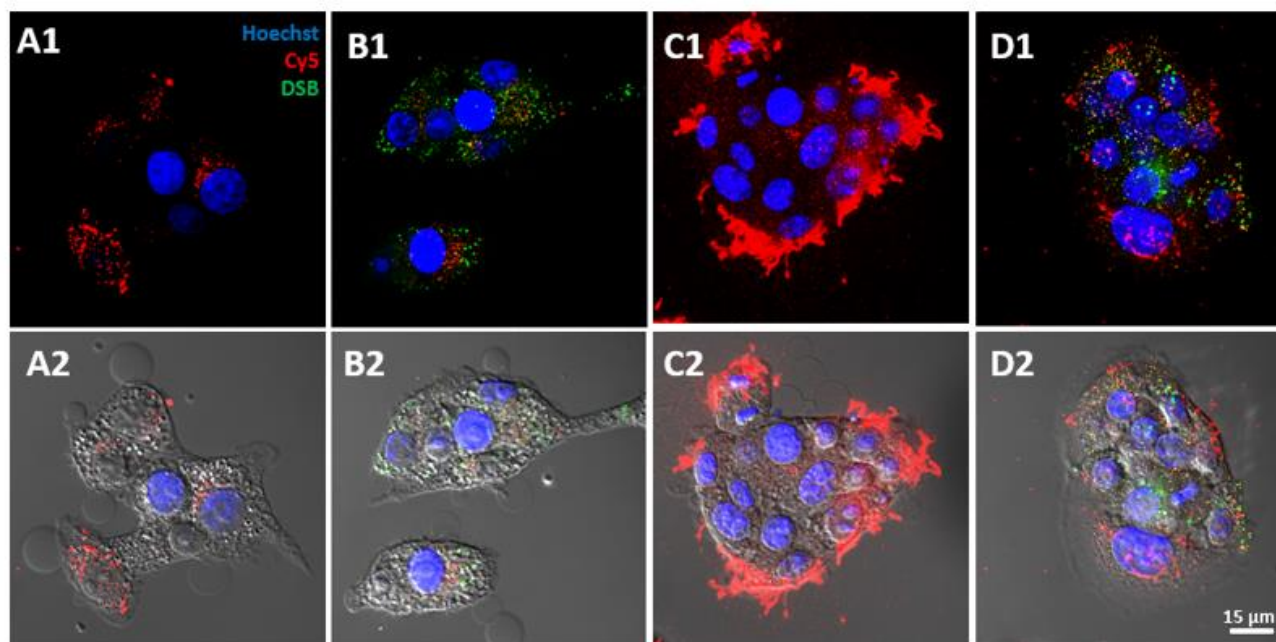


Figure 7. Cellular uptake of HA-m-poly(DAAM-co-DMA) crosslinked nanogels by HeLa cells (Fig. 7 A and B) and TS/A pc cells (Fig. 7 C and D). Confocal microscopy images of HeLa and TS/A-pc cells incubated for 16 h only with Cya5-labelled crosslinked nanogels (A and C, respectively) and DSB-loaded Cya5-labelled crosslinked nanogels (B and D, respectively). The upper panels show only the fluorescence channels. The lower panel depicts an additional overlay with the DIC channel. Cell nucleus was stained blue with Hoechst, DSB is visualized in the green fluorescence channel and cyanine5 in the red fluorescence channel.

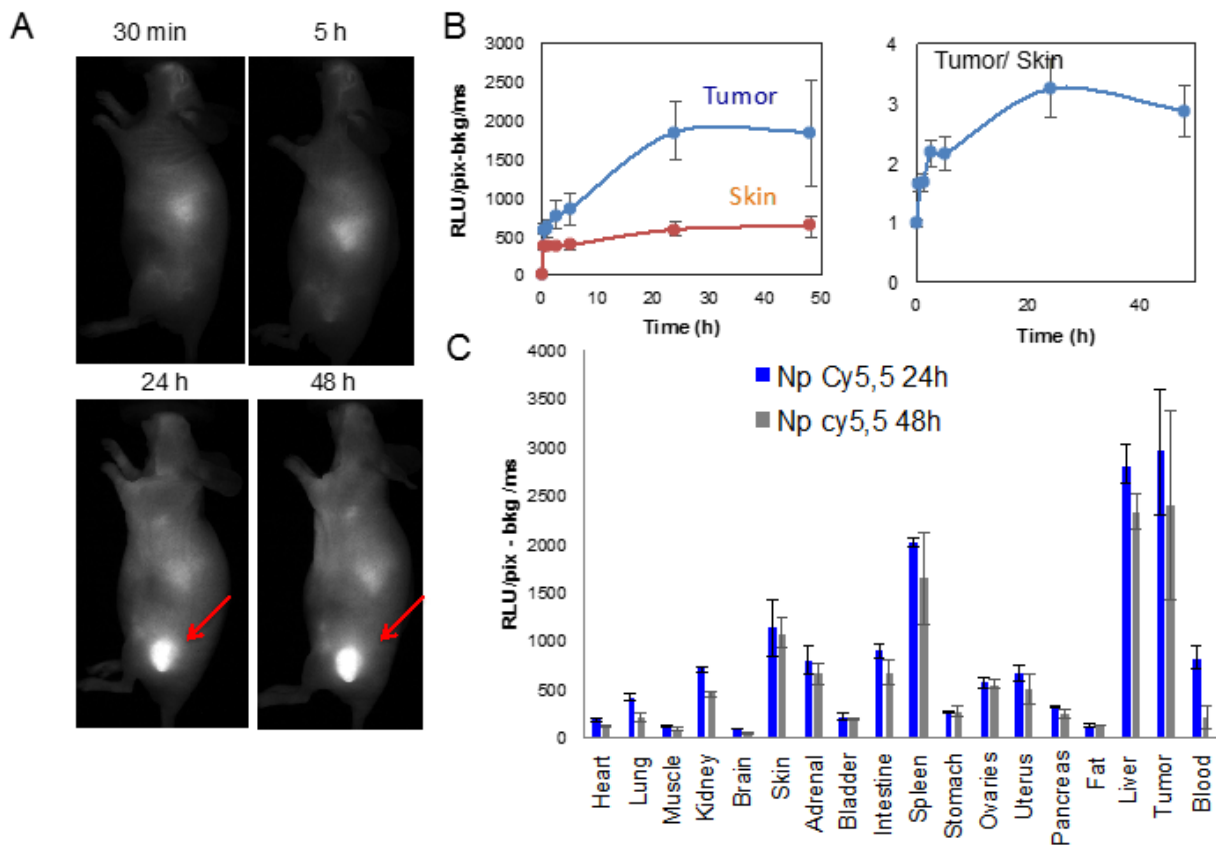


Figure 8. (A) *In vivo* near-infrared fluorescence (NIRF) images of the time dependant biodistribution of Cy5.5-labeled crosslinked nanogels in TSA-pc (murine breast cancer) tumor-bearing mice. The tumor locations are indicated by the arrows. (B) Representative ex vivo fluorescence quantification of dissected skin and tumor. (C) Quantification of the ex vivo tumor targeting characteristics of Cy5.5-labeled crosslinked nanogels in TSA-pc tumor-bearing mice. ROIs were defined on the extracted organs to semi-quantify the amount of photons detected per pixel after a 200 ms exposure. The results in each organ are expressed as the mean \pm SD.

Supporting information

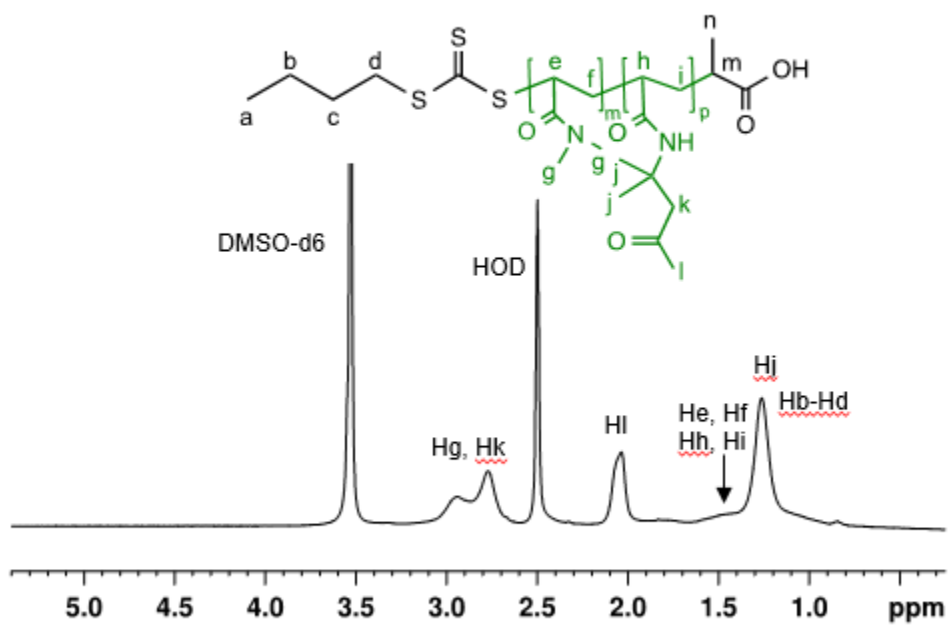


Figure SI-1. ¹H NMR spectrum (400 MHz, 6 mg/mL in DMSO-d₆, 10 °C) of the copolymer poly(DAAM-co-DMA).

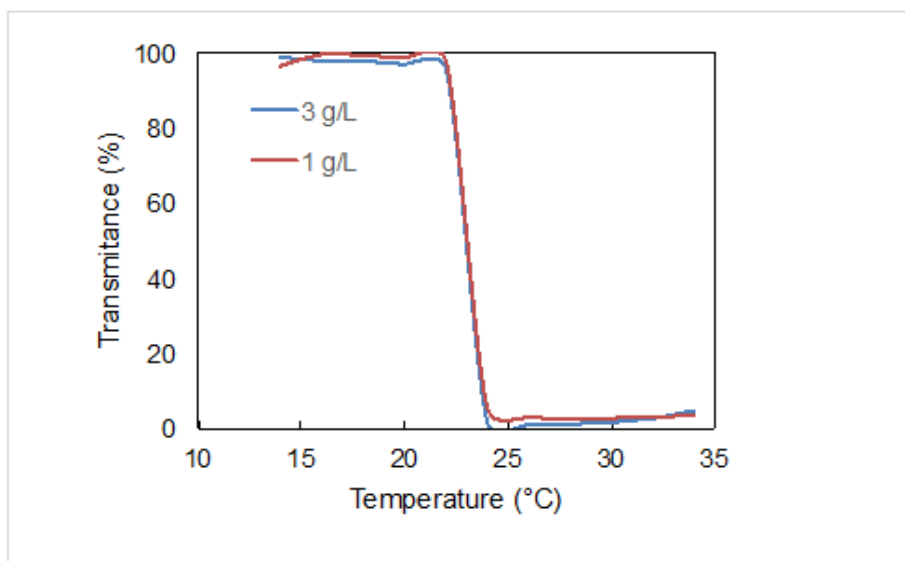


Figure SI-2. Phase transition of poly(DAAM-co-DMA) in PBS at 1 and 3 g/L as measured by UV/Vis spectroscopy at 500 nm. The cloud point temperature was found to be 24°C for the two concentrations tested.

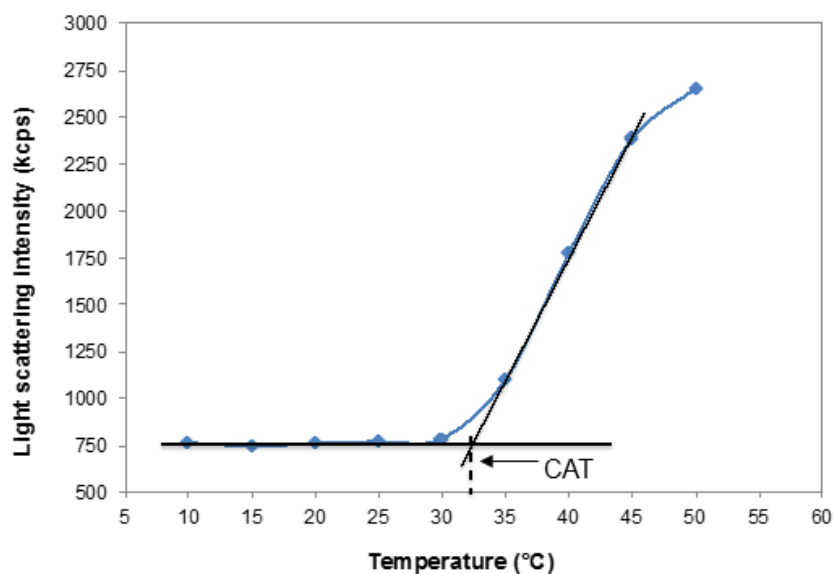


Figure SI-3. Light scattering intensity of a solution of HA-m-poly(DAAM-co-DMA) in PBS at 0.5 g/L as a function of temperature. The critical aggregation temperature was found to be 32 °C.